







ARTICLE

A novel dual Ca²⁺ sensor system regulates Ca²⁺-dependent neurotransmitter release

Lei Li^{1*}, Haowen Liu^{1*}, Mia Krout² , Janet E. Richmond² , Yu Wang³, Jihong Bai³ , Saroja Weeratunga⁴, Brett M. Collins⁴ , Donovan Ventimiglia⁵, Yi Yu¹, Jingyao Xia¹, Jing Tang¹, Jie Liu⁶ , and Zhitao Hu¹ 

Ca²⁺-dependent neurotransmitter release requires synaptotagmins as Ca²⁺ sensors to trigger synaptic vesicle (SV) exocytosis via binding of their tandem C2 domains—C2A and C2B—to Ca²⁺. We have previously demonstrated that SNT-1, a mouse synaptotagmin-1 (Syt1) homologue, functions as the fast Ca²⁺ sensor in *Caenorhabditis elegans*. Here, we report a new Ca²⁺ sensor, SNT-3, which triggers delayed Ca²⁺-dependent neurotransmitter release. *snt-1;snt-3* double mutants abolish evoked synaptic transmission, demonstrating that *C. elegans* NMJs use a dual Ca²⁺ sensor system. SNT-3 possesses canonical aspartate residues in both C2 domains, but lacks an N-terminal transmembrane (TM) domain. Biochemical evidence demonstrates that SNT-3 binds both Ca²⁺ and the plasma membrane. Functional analysis shows that SNT-3 is activated when SNT-1 function is impaired, triggering SV release that is loosely coupled to Ca²⁺ entry. Compared with SNT-1, which is tethered to SVs, SNT-3 is not associated with SV. Eliminating the SV tethering of SNT-1 by removing the TM domain or the whole N terminus rescues fast release kinetics, demonstrating that cytoplasmic SNT-1 is still functional and triggers fast neurotransmitter release, but also exhibits decreased evoked amplitude and release probability. These results suggest that the fast and slow properties of SV release are determined by the intrinsically different C2 domains in SNT-1 and SNT-3, rather than their N-termini-mediated membrane tethering. Our findings therefore reveal a novel dual Ca²⁺ sensor system in *C. elegans* and provide significant insights into Ca²⁺-regulated exocytosis.

Introduction

At the presynaptic nerve terminal, synaptic vesicles (SVs) fuse with the plasma membrane to release neurotransmitters, a process triggered by Ca²⁺ binding to Ca²⁺ sensor proteins (Chapman, 2008; Südhof, 2012). Several synaptotagmin (Syt) family proteins have been recognized as Ca²⁺ sensors in both vertebrates and invertebrates (Lee et al., 2013; Li et al., 2018; Mackler et al., 2002; Nishiki and Augustine, 2004; Wen et al., 2010; Xu et al., 2007; Xu et al., 2009; Yoshihara and Littleton, 2002). All known Syt Ca²⁺ sensors (e.g., Syt1, Syt2, Syt7, and Syt9) have a similar structure that consists of tandem C2 domains—C2A and C2B—that generally use comparable Ca²⁺-binding mechanisms, and an N-terminal transmembrane domain (TM) that tethers Syts to distinct cellular compartments. Apart from their Ca²⁺-binding ability, the C2 domains also interact with the SNARE complex and the plasma membrane to promote fusion (Chapman et al., 1995; Chapman and Jahn, 1994; Sutton et al., 1995; Zhang et al., 2002).

To trigger the exocytosis of SVs, many mammalian neurons employ at least two Ca²⁺ sensors. Syt1 or Syt2 functions as the fast Ca²⁺ sensor to trigger fast synchronous release, and Syt7 functions as the slow Ca²⁺ sensor to mediate slow asynchronous release (Bacaj et al., 2013; Chen et al., 2017a; Chen et al., 2017b; Kochubey and Schneggenburger, 2011; Luo et al., 2015; Schonn et al., 2008; Weber et al., 2014; Wen et al., 2010). Simultaneous ablation of both Syt1 and Syt7 almost completely abolishes stimulus-evoked neurotransmitter release at these synapses (Bacaj et al., 2013). In other neuron types, such as the calyx of Held and parvalbumin-expressing inhibitory neurons, Syt1 and Syt2 are coexpressed and regulate fast neurotransmitter release redundantly (Bouhours et al., 2017; Kochubey et al., 2016). In addition to triggering slow, asynchronous release, Syt7 is also involved in the regulation of synaptic facilitation and vesicle pool replenishment (Chen et al., 2017b; Jackman et al., 2016) and

¹Queensland Brain Institute, Clem Jones Centre for Ageing Dementia Research, The University of Queensland, Brisbane, Queensland, Australia; ²Department of Biological Sciences, University of Illinois at Chicago, Chicago, IL; ³Division of Basic Sciences, Fred Hutchinson Cancer Research Center, Seattle, WA; ⁴Institute for Molecular Bioscience, The University of Queensland, Brisbane, Queensland, Australia; ⁵Lulu and Anthony Wang Laboratory of Neural Circuits and Behavior, The Rockefeller University, New York, NY; ⁶Neuroscience Program, Monash Biomedicine Discovery Institute and Department of Anatomy and Developmental Biology, Monash University, Melbourne, Victoria, Australia.

*L. Li and H. Liu contributed equally to this paper; Correspondence to Zhitao Hu: z.hu1@uq.edu.au; D. Ventimiglia's present address is Molecular Neurobiology Laboratory, The Salk Institute for Biological Studies, La Jolla, CA.

© 2021 Li et al. This article is distributed under the terms of an Attribution–Noncommercial–Share Alike–No Mirror Sites license for the first six months after the publication date (see <http://www.rupress.org/terms/>). After six months it is available under a Creative Commons License (Attribution–Noncommercial–Share Alike 4.0 International license, as described at <https://creativecommons.org/licenses/by-nc-sa/4.0/>).

confers frequency invariance in some depressing synapses (Turecek et al., 2017).

Both fast and slow Ca^{2+} sensors possess an N-terminal TM domain that tethers the sensor to either SVs or the plasma membrane (Brose et al., 1992; Littleton et al., 1993; Perin et al., 1990; Sugita et al., 2001); however, the functional importance of the membrane tethering of Ca^{2+} sensors remains controversial. It has been reported that the cytoplasmic domain of Syt1 is fully functional in an in vitro membrane fusion assay (Wang et al., 2011) and facilitates exocytosis when injected into crayfish motor neurons (Hua et al., 2014). Moreover, tethering the C2 domains of Syt1 to the plasma membrane fully restored fast synchronous release in Syt1 knockout neurons (Hui et al., 2009); however, Syt1 that lacked the TM domain failed to restore fast synchronous release in *Drosophila* Syt1 mutants (Lee and Littleton, 2015). These conflicting findings raise the important question of how the functions of dual-system fast and slow Ca^{2+} sensors rely on their membrane tethering in triggering SV release.

We have previously demonstrated that SNT-1, an Syt1 homologue, functions as a Ca^{2+} sensor for Ca^{2+} -dependent fast neurotransmitter release at the *Caenorhabditis elegans* neuromuscular junction (NMJ; Li et al., 2018; Yu et al., 2013). Here, we provide evidence that SNT-3 acts as an additional Ca^{2+} sensor that triggers delayed evoked neurotransmitter release at the worm NMJ. *snt-3* belongs to the worm synaptotagmin gene family; however, it lacks an N-terminal sequence including the TM domain, which differentiates it from all other Syt Ca^{2+} sensors. Functional analysis revealed that the SV fusion mediated by SNT-1 and SNT-3 differs in synaptic properties in terms of Ca^{2+} sensitivity, release kinetics, synaptic depression, and synaptic refilling. Remarkably, altering the membrane tethering of SNT-1 did not affect the fast release properties. Thus, the functions of these two Ca^{2+} sensors are mainly determined by their intrinsically distinct C2 domains. Our findings provide evidence of a novel, dual Ca^{2+} sensor system for synaptic transmission and shed light on the molecular mechanisms by which Syts regulate fast and slow neurotransmitter release.

Results

SNT-3 is required for delayed evoked neurotransmitter release

Numerous studies have shown that Syt1 functions as a Ca^{2+} sensor that triggers fast synchronous neurotransmitter release (Geppert et al., 1994; Lee et al., 2013; Li et al., 2018; Nishiki and Augustine, 2004). The *C. elegans* genome encodes seven Syt genes, including *snt-1*, *snt-2*, *snt-3*, *snt-4*, *snt-5*, *snt-6*, and *snt-7* (Fig. S1). Of these Syt isoforms, only SNT-1 has been proven to be a Ca^{2+} sensor that triggers fast neurotransmitter release (Li et al., 2018) by using a mechanism analogous to that of Syt1, indicative of an evolutionarily conserved function of Syt1 across species. Despite the functional importance of SNT-1, delayed evoked release is still observed in *snt-1* mutants, implying that multiple Ca^{2+} sensors are required for SV release.

To identify additional Ca^{2+} sensor(s) in *C. elegans*, we performed a behavioral screen of other Syt genes in the *snt-1* mutant background and found that locomotion speed was dramatically reduced in *snt-1*;*snt-3* double mutants (two *snt-3* alleles were

used: *tm5776*, a 322-bp deletion, and *ky1034*, an early stop codon in the first exon; Fig. 1 A), suggesting that SNT-3 may be involved in the regulation of SV release in *snt-1* mutants. Behavioral analysis in *snt-3* single mutants revealed a slight but significant decrease in locomotion speed (Fig. 1, B and C), which was restored by either a single copy insertion or pan-neuronal overexpression of SNT-3 cDNA (using the *rab-3* promoter). Moreover, the locomotion of *snt-1*;*snt-3* double mutants was also restored to the same level as that of *snt-1* single mutants by overexpression of SNT-3 (Fig. 1, B and C), demonstrating that the *snt-3* cDNA is fully functional in the nervous system. In addition to the defect in locomotion, the *snt-1*;*snt-3* double mutant worms also exhibited severely reduced body length, whereas the *snt-3* single mutants were comparable to WT worms (Fig. S2).

We next analyzed SV release by measuring evoked excitatory postsynaptic currents (EPSCs) in *snt-3* single mutants and *snt-1*;*snt-3* double mutants. Consistent with the profound locomotion defect, evoked EPSCs were completely eliminated in *snt-1*;*snt-3* double mutants (Fig. 1 D), demonstrating that SNT-3 is required for SV release in the absence of SNT-1. Despite the slight decrease in their locomotion speed, the *snt-3* single mutants displayed normal evoked EPSC amplitude, charge transfer, and release kinetics. In contrast, *snt-1* single mutants exhibited a delayed latency to evoked EPSC onset, as well as reduced EPSC amplitude and charge transfer (Fig. 1, D–F). Neuronal expression of *snt-3* cDNA in *snt-1*;*snt-3* double mutants restored the evoked EPSCs to 90% of the level in *snt-1* mutants. These results demonstrate that evoked neurotransmitter release at the worm NMJ requires both SNT-1 and SNT-3, which mediate fast and delayed neurotransmitter release, respectively.

To determine whether SNT-3 is required for tonic release, we measured miniature EPSCs (mEPSCs). The mEPSC frequency was reduced by 85% in *snt-1* mutants (Fig. 1, G and H), demonstrating the importance of SNT-1 in triggering tonic release, which is consistent with our previous findings (Li et al., 2018). In contrast, the mEPSC frequency was unchanged in *snt-3* single mutants compared with WT, as well as in *snt-1*;*snt-3* double mutants compared with *snt-1* single mutants (Fig. 1, G and H), indicating that SNT-3 is not required for tonic release. Loss of *snt-1* or *snt-3* did not result in a change in mEPSC kinetics (Fig. S3), demonstrating that the function of the postsynaptic acetylcholine receptors (AChRs) is normal in these mutants. Of note, the mEPSC amplitude was increased in *snt-1* mutants (Fig. 1 H), likely reflecting a role for SNT-1 in endocytosis, consistent with previous studies and the ultrastructural analyses in Fig. 4 and Fig. S6 (Jorgensen et al., 1995; Yu et al., 2013). The increased mEPSC amplitude in *snt-1* mutants was suppressed in *snt-1*;*snt-3* double mutants (Fig. 1 H and Fig. S4), suggesting that SNT-3 may also regulate endocytosis, a finding that is further supported by EM analysis (Fig. 4). Collectively, these results demonstrate that SNT-3 triggers a delayed component of evoked neurotransmitter release, revealed in the absence of the fast Ca^{2+} sensor SNT-1, likely by acting as a second Ca^{2+} sensor.

C2 domains of SNT-3 and SNT-1 exhibit sequence similarity

Like all other Syts, SNT-3 contains tandem C2 domains (C2A and C2B; Fig. 2 A). Sequence analysis showed that the C2 domains in

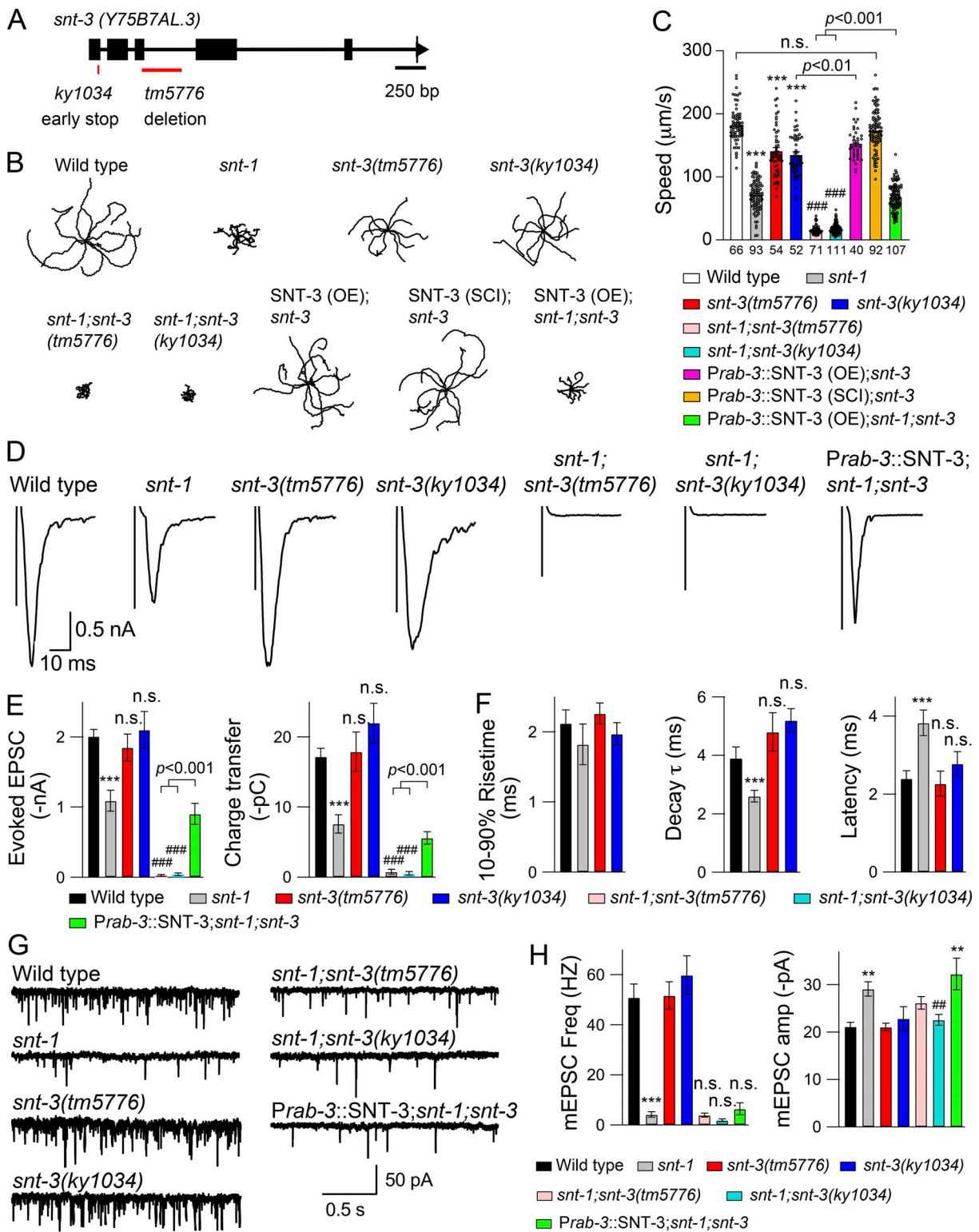


Figure 1. SNT-3 mediates evoked neurotransmitter release in the absence of SNT-1. (A) Schematic of the *snt-3* gene. Black boxes represent the coding exons. The *ky1034* early stop codon and the *tm5776* deletion were indicated. (B) Representative locomotory trajectories of 10 animals for each indicated genotypes, including WT, *snt-1*, *snt-3(tm5776)*, *snt-3(ky1034)*, *snt-1;snt-3(tm5776)*, *snt-1;snt-3(ky1034)*, SNT-3 rescue by overexpression (OE) and single-copy insertion (SCI) in *snt-3* single mutants, and SNT-3 overexpression rescue in *snt-1;snt-3* double mutants. The starting points of each trajectory have been aligned for clarity. (C) Quantification of the average locomotion speed for the indicated genotypes or transgenes in B. Data are mean ± SEM. ***P < 0.001 compared with WT; ###P < 0.001 compared with *snt-1* mutants. n.s., nonsignificant compared with WT (one-way ANOVA). (D) Example traces of evoked EPSCs recorded from body wall muscle. (E) Summary of the mean amplitude and charge transfer of the evoked EPSCs in D. Data are mean ± SEM. ***P < 0.001 compared with WT; ###P < 0.001 compared with *snt-1* mutants. n.s., nonsignificant compared with WT (one-way ANOVA). (F) Quantifications of the rise time, decay, and latency of evoked EPSCs. Data are mean ± SEM. ***P < 0.001 compared with WT. n.s., nonsignificant compared with WT (one-way ANOVA). (G) Representative mEPSC traces. (H) Quantification of the mEPSC frequency and amplitude for the indicated genotypes. Data are mean ± SEM. ***P < 0.001 compared with WT; ###P < 0.001 compared with *snt-1* mutants. n.s., nonsignificant compared with WT (one-way ANOVA).

following Kruskal-Wallis test). **(G)** Representative traces of mEPSCs. **(H)** Summary of the mean frequency and amplitude of the mEPSCs for each genotype or transgene. Data are mean \pm SEM. ** $P < 0.01$, *** $P < 0.001$ compared with WT; ## $P < 0.01$, compared to *snt-1* mutants; n.s., nonsignificant compared with *snt-1* mutants (one-way ANOVA).

SNT-3 share a high level of identity with those in SNT-1 and Syt1. The SNT-3 C2A domain shares 67.3% identity with the SNT-1 C2A domain, as well as 68.8% identity with the Syt1 C2A domain. The C2B domain shares 62.1% identity with the SNT-1 C2B domain, as well as 62.9% identity with the Syt1 C2B domain. Moreover, the five canonical aspartates are all conserved in the C2A domain of SNT-3 (Fig. 2 B, aspartates, blue), and the C2B domain possesses four aspartates, with the fifth being replaced by glutamate (Fig. 2 B, red). Despite the high similarity of the C2 domains of SNT-3 and SNT-1, SNT-3 lacks an N-terminal TM domain, unlike all other known Ca^{2+} sensors in the Syt family, encoding a very short N-terminal sequence of only 11 aa (Fig. 2, A and B). Among the 17 Syts in mouse, only Syt17 lacks a TM domain, but it is not involved in SV exocytosis (Ruhl et al., 2019). Thus far, our findings in relation to SNT-3 suggest that a TM domain may not be indispensable for a Syt to trigger SV release.

SNT-3 is localized to synaptic regions in cholinergic synapses

To examine the expression pattern of *snt-3*, an mApple reporter driven by an *snt-3* promoter (5 kb upstream region) was generated. Expression was observed in a large number of neurons in the head, tail, and ventral and dorsal nerve cords (Fig. 2 C, C1–C6), including nearly all cholinergic and GABAergic motor neurons (Fig. 2 D, D1–D6), indicating a broad role for SNT-3 in the nervous system. Expression of *snt-3* was also found in head and body wall muscles (Fig. 2 C), implying that SNT-3 may also serve a postsynaptic function at NMJs. Postsynaptic AChRs appeared to function normally, as puffing acetylcholine (ACh; 0.5 M, 100 ms) onto the body wall muscle produced similar evoked currents in WT and *snt-3* mutants (Fig. S5).

To examine the subcellular localization of SNT-3, we constructed an SNT-3::mApple fusion protein and expressed it in the D-type cholinergic motor neurons (under the *unc-129* promoter; Li et al., 2019; McEwen et al., 2006). Compared with RAB-3::GFP (labeling SVs) and SNT-1::GFP, SNT-3::mApple displayed a relatively diffuse distribution in axons. Although boutons could be observed (Fig. 2 E, E2 and E5, arrows), the fluorescence in these regions was not as bright as that observed with RAB-3::GFP and SNT-1::GFP. This suggests that SNT-3 and SNT-1 may have differential cellular localization.

The N-terminal TM domain in Syt1 is embedded in the vesicular membrane, tethering Syt1 to SVs (Brose et al., 1992; Matthew et al., 1981). The conserved TM domain in SNT-1 and the colocalization of SNT-1 with SV markers suggest that SNT-1 is also localized on SVs (Li et al., 2018), whereas the lack of a TM domain in SNT-3 and diffuse neuronal expression indicates that it is not localized in this manner. It has been reported that synaptic proteins located on SVs become more punctate in mutants with defective SV exocytosis, such as *unc-13* mutants (McEwen et al., 2006). Similar changes were observed with

SNT-1::GFP, which exhibited a standard synaptic distribution in WT animals, but became more punctate in *unc-13* mutants (s69; Fig. 2 F, F1 and F2). The percentage of bouton fluorescence to total axonal fluorescence of SNT-1::mApple was significantly increased in *unc-13* mutants (Fig. 2 F, F5). In contrast, the distribution of SNT-3::mApple showed no apparent change in *unc-13* mutants (Fig. 2 F, F3–F5), suggesting that SNT-3 is not localized on SVs.

To further examine the relationship between SVs and SNT-1 or SNT-3, we analyzed the distribution of SNT-1::mApple and SNT-3::mApple—both under the *unc-129* promoter, which drives expression in D-type cholinergic motor neurons that send projections from ventral cord cell bodies to form synapses along the dorsal nerve cord—in *unc-104* KIF1A mutants. *unc-104* encodes a kinesin required for axonal transport of SV proteins in both *C. elegans* and mice (Hall and Hedgecock, 1991; Okada et al., 1995; Otsuka et al., 1991). As shown in Fig. 2 G (G1 and G2), dorsal nerve cord axonal fluorescence of SNT-1::mApple (arrow) was virtually undetectable in *unc-104* KIF1A mutants compared with WT (Fig. 2 G, G5). This was accompanied by a marked increase in SNT-1::mApple fluorescence in the cell bodies of D-type neurons in the ventral cord (star), as observed previously (Mullen et al., 2012). This indicates that the subcellular distribution of SNT-1 is coupled to anterograde transport of SV precursors. In contrast, the SNT-3::mApple fluorescence in both axons and cell bodies in *unc-104* KIF1A mutants was comparable to that in WT animals (Fig. 2 G, G3–G5), suggesting that the SNT-3 expression pattern does not depend on the SV kinesin UNC-104. Taken together, these results indicate that SNT-3, in contrast to SNT-1, is not associated with SVs.

SNT-3 exhibits Ca^{2+} and membrane binding properties

To determine the Ca^{2+} -binding properties of the SNT-3 C2 domains, we performed isothermal titration calorimetry (ITC) experiments with recombinantly expressed and purified SNT-3 C2 domains. Our results revealed that the SNT-3 C2 domains bind to Ca^{2+} with an affinity of $46.6 \pm 2.7 \mu\text{M}$ ($n = 3$) at 25°C (Fig. 3, A and B). The relatively weak Ca^{2+} -binding affinity of SNT-3 suggests that it may have a similar function to mammalian Syt isoforms, acting as a regulatory protein in Ca^{2+} -dependent cellular exocytosis.

To determine whether SNT-3 C2 domains possess Ca^{2+} -dependent membrane binding activity, we next performed a liposome cosedimentation assay. The cytoplasmic domain (C2AB) of SNT-1 was used as a positive control. Our results showed that WT C2AB of either SNT-1 or SNT-3 cosedimented with liposomes (25%PS/75%PC) in the presence of 1 mM Ca^{2+} ; however, in the absence of Ca^{2+} (1 mM EGTA), no significant levels of C2AB membrane binding were detected (Fig. 3, C and D). Mutations that disrupt the Ca^{2+} -binding sites in the C2 domain of SNT-1 or SNT-3 (SNT-1 C2AB D3,4N; SNT-3 C2AB D3,4N) abolished the Ca^{2+} -dependent interactions with liposomes (Fig. 3, C and D). Together, these results demonstrate that SNT-3, similar

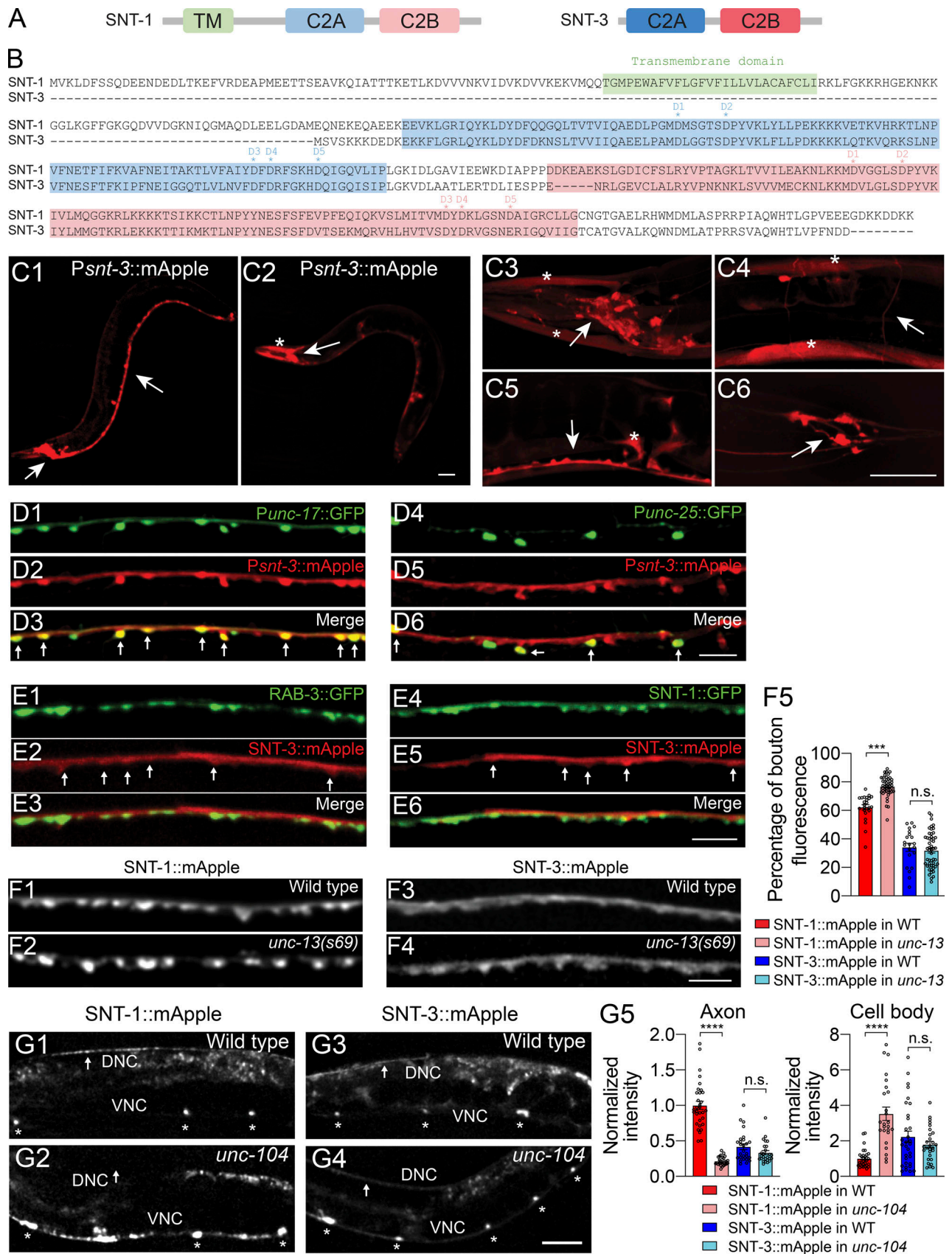


Figure 2. Expression pattern and subcellular localization of SNT-3 in cholinergic motor neurons. (A and B) Domain structure and sequence alignment of the SNT-1 and SNT-3. The transmembrane domain (green), the C2A domain (light blue), and the C2B domain (light red) are highlighted. (C1–C6) Expression of *snt-3* driven by the endogenous *snt-3* promoter in various regions (arrow, neuron; star, muscle), including head neurons, tail neurons, motor neurons, head

muscles, and body wall muscles. Scale bar, 50 μm . **(D1–D6)** Expression *snt-3* (driven by the *snt-3* promoter; red) in both cholinergic and GABAergic motor neurons (driven by the *unc-17* and *unc-25* promoters, respectively; green) at the ventral nerve cord. Scale bar, 20 μm . **(E1–E6)** Fluorescent images of the dorsal nerve cord (under the *unc-129* promoter) showing colocalization of SNT-3::mApple with Rab3::GFP (SV marker) and SNT-1::GFP. Scale bar, 5 μm . **(F1–F4)** Expression patterns of SNT-1::mApple and SNT-3::mApple in WT and *unc-13(s69)* mutant background, respectively. Scale bar, 5 μm . **(F5)** Averaged percentage of the bouton fluorescence to the total axonal fluorescence of SNT-1::mApple and SNT-3::mApple in WT and *unc-13* mutants. Data are mean \pm SEM. *** $P < 0.001$. n.s., nonsignificant (one-way ANOVA). **(G1–G4)** Distribution of SNT-1::mApple and SNT-3::mApple in the dorsal or ventral nerve cords of WT and *unc-104* KIF1A mutants are compared. SNT-1::mApple axonal fluorescence (dorsal nerve cord [DNC]) decreased, while cell body fluorescence (ventral nerve cord [VNC]) increased in *unc-104* mutants, whereas SNT-3::mApple axonal fluorescence and cell body fluorescence were comparable between WT and *unc-104* mutants. Stars indicate the cell bodies in VNC, and arrows indicate axons in DNC. Scale bar, 5 μm . **(G5)** Quantification of somatic and axonal fluorescence intensity of SNT-1::mApple and SNT-3::mApple in WT and *unc-104* mutants. Data are mean \pm SEM. **** $P < 0.0001$. n.s., nonsignificant (one-way ANOVA).

to SNT-1, also has a Ca^{2+} -dependent phospholipid binding activity.

Differential roles of SNT-1 and SNT-3 in SV docking and priming

To become fusion competent, SVs must undergo docking and priming (Becherer and Rettig, 2006; Rizo and Rosenmund, 2008; Verhage and Sørensen, 2008). Knockout of fast and slow Ca^{2+} sensors may directly influence these upstream processes, thereby causing defects in the final fusion step. To investigate this, the synaptic ultrastructure of WT, *snt-1*, *snt-3*, and *snt-1;snt-3* double mutants was examined following high-pressure freeze fixation and freeze substitution, a method that preserves synaptic architecture in its near native state (Weimer et al., 2006). Morphometric analyses of ventral cord cholinergic synapses revealed multiple differences between these genotypes (Fig. 4

A). The total number of docked SVs was not significantly reduced in *snt-1* mutants, but was significantly increased in both *snt-3* single mutants and *snt-1;snt-3* double mutants (Fig. 4 B). Previous studies have identified distinct docked vesicle pools at these synapses. Specifically, SVs proximal to the dense projection (DP; <90 nm) are docked by interactions between vesicle-associated RAB-3 and DP localized UNC-10 (RIM–Rab-3-interacting molecule), require the long isoform of UNC-13 to become primed, and exhibit release kinetics tightly coupled to Ca^{2+} -entry (Gracheva et al., 2008; Hammarlund et al., 2007; Weimer et al., 2006). More distally docked SVs (90–300 nm) require the short UNC-13MR isoform and exhibit slower release kinetics with loose Ca^{2+} -coupling (Hu et al., 2013). Given the different kinetics of SNT-1- and SNT-3-dependent evoked release, we examined the distribution of docked SVs relative to the DP. This analysis revealed a significant reduction in the number of proximally docked

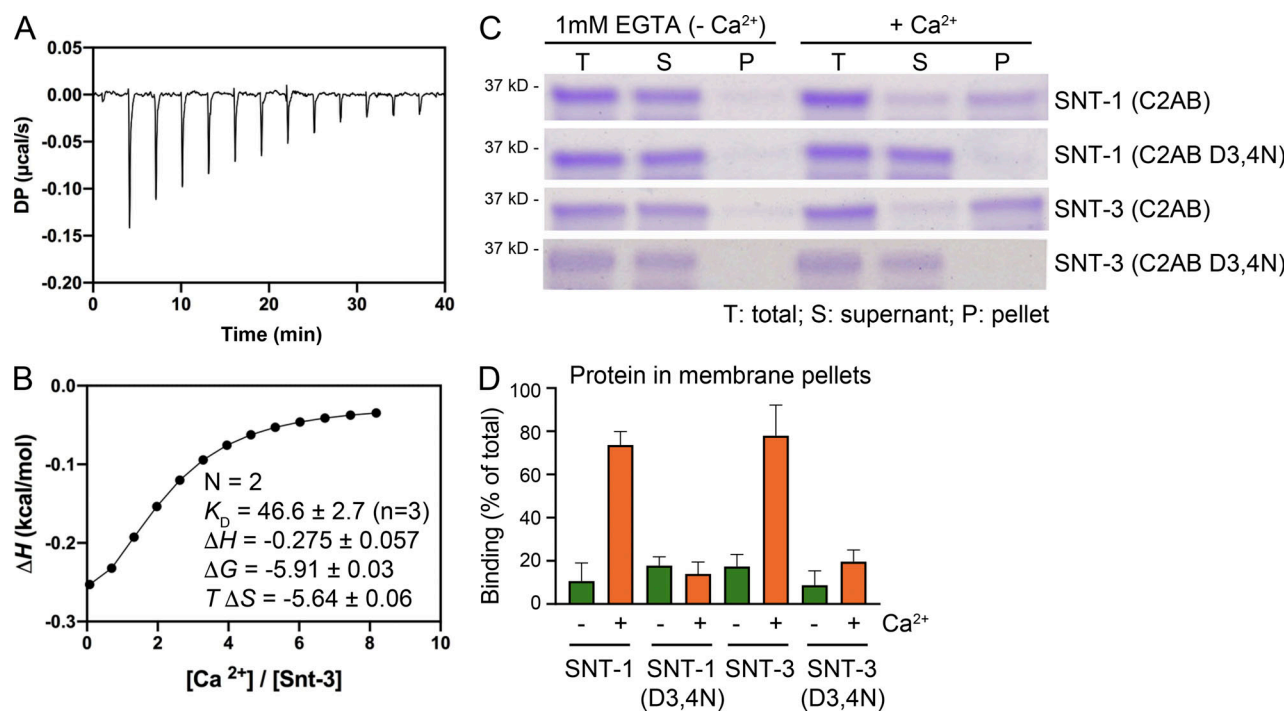


Figure 3. SNT-3 binds Ca^{2+} and membranes. (A and B) The Ca^{2+} -binding properties of SNT-3 were measured by ITC; raw data (A) and integrated and normalized data (B) fitted with a 1:1 binding model. The average binding affinity (dissociation constant [K_D]) was calculated by carrying out three independent titrations. **(C and D)** Ca^{2+} -dependent membrane interactions of WT and mutant versions of SNT-1 C2AB and SNT-3 C2AB were determined with liposome cosedimentation experiments. Representative images of SDS-PAGE gels are shown in C. “ $+\text{Ca}^{2+}$ ” indicates 1 mM Ca^{2+} , and “ $-\text{Ca}^{2+}$ ” indicates 1 mM EGTA. The percentage of protein in pellets was quantified by using ImageJ and plotted in D. Cosedimentation experiments were independently repeated five times for SNT-1 C2AB and four times for SNT-3 C2AB variants.

SVs in *snt-1* mutants, but not *snt-3* mutants, which was consistent with the notion that SNT-1 may stabilize SV docking in this region (Fig. 4 C and Fig. S6 A). Conversely, the distally docked SV pool was significantly increased in *snt-3* mutants, suggesting that, in the absence of SNT-3, release of the distal docked SV pool is impeded (Fig. 4 D and Fig. S6 A). Docked SVs beyond the distal pool (300–500 nm) are known to accumulate in some endocytic mutants (Wang et al., 2008). In *snt-1* mutants, a significant increase in this pool was observed (Fig. 4 E and Fig. S6 A). Furthermore, *snt-1* mutants exhibited reduced SV number and increased SV diameters, and accumulated irregular vesicles defined by thicker membranes and clear lumens, all of which are indicative of vesicle recycling defects, as previously reported (Jorgensen et al., 1995; Yu et al., 2013; Fig. 4, F–H; and Fig. S6, B and D). In contrast, *snt-3* single mutants exhibited WT levels of SVs and irregular vesicles, but had reduced SV diameters and terminal areas (Fig. 4, F–I). In the *snt-1*;*snt-3* double mutants, SV numbers were restored to WT levels, possibly accumulating due to the lack of release (Fig. 4 F). The number of docked vesicles in the endocytic zone trended higher than the WT and irregular vesicles accumulated, suggesting that SNT-1 endocytosis was still impaired in the double mutants (Fig. 4, E and H; and Fig. S6 A). However, the terminal area, SV diameter, and size of irregular vesicles were reduced relative to WT and *snt-1* single mutants (Fig. 4, G–I; and Fig. S6, B and D). Together, these observations suggest that SNT-1 and SNT-3 have different roles in both vesicle docking and recycling.

To directly assess whether these morphological changes in SV docking impact priming, we next assayed the readily releasable pool (RRP) of SVs by measuring the total charge transfer produced by a pulsed application of hypertonic sucrose (1 M, 2 s) onto the ventral nerve cord. This assay has been widely used for the estimation of the RRP in both vertebrates and invertebrates (Li et al., 2019; Liu et al., 2019; Richmond et al., 1999; Rosenmund and Stevens, 1996). Our results showed that the charge transfer of the sucrose response was unchanged in both *snt-1* and *snt-3* mutants, but was significantly reduced in *snt-1*;*snt-3* double mutants (Fig. 4, J and K). We next analyzed the quantal content of the RRP, which was calculated by ratioing the total charge transfer of the sucrose-evoked current to the average mEPSC charge transfer. For *snt-1* mutants, the mEPSC charge transfer was significantly increased, likely reflecting the right-shifted SV diameter histogram and the corresponding increase in the frequency of abnormally large amplitude mEPSCs (Fig. 4, H and L; and Fig. S6, B–D). The larger mEPSC charge transfer of *snt-1* mutants leads to a 30% decrease in the calculated quantal content (Fig. 4, L and M). These results indicate a role for SNT-1 in priming, in agreement with previous observations (Chang et al., 2018; Courtney et al., 2019; Li et al., 2018; Liu et al., 2009a). We did not observe a change in the mEPSC charge transfer in *snt-3* mutants, probably because the decrease in vesicle size was minimal, leading to WT estimates of quantal content (Fig. 4, L and M). However, because *snt-1*;*snt-3* double mutants exhibited a more pronounced reduction in SV size and smaller irregular vesicles, the mEPSC charge transfer was closer to WT (Fig. 4, H and L; and Fig. S6, B and D). Consequently, the calculation of quantal content in *snt-1*;*snt-3* double mutants was markedly reduced (~50%) compared with WT, but comparable to that in

snt-1 single mutants (Fig. 4 M). These results indicate that SV priming is partially suppressed by the simultaneous loss of SNT-1 and SNT-3. Given that evoked release is completely eliminated, these data further suggest that both SNT-1 and SNT-3 have additional functions downstream of priming in Ca²⁺-triggered release.

SVs mediated by SNT-3 have loose coupling to Ca²⁺ entry

The above experiments suggest that SNT-3 may function as a second Ca²⁺ sensor in the absence of SNT-1. The prolonged latency in the evoked EPSCs when SNT-3 is the primary Ca²⁺ sensor (i.e., in *snt-1* mutants) indicates that SNT-3 mediates delayed neurotransmitter release. These observations reveal a dual Ca²⁺ sensor system in *C. elegans* that utilizes SNT-1 and SNT-3 to trigger Ca²⁺-dependent neurotransmitter release, analogous to Syt1 and Syt7, which are employed for fast synchronous and slow asynchronous release at specific murine synapses (Bacaj et al., 2013; Wen et al., 2010).

We next examined whether the SV release mediated by the two Ca²⁺ sensors exhibits differential synaptic properties, such as Ca²⁺ dependence. Evoked EPSCs were compared in the presence of 1 mM and 0.5 mM Ca²⁺ in WT, *snt-3*, and *snt-1* mutants. Decreasing the Ca²⁺ concentration from 1 mM to 0.5 mM significantly reduced evoked EPSC amplitude and charge transfer by 50% in both WT and *snt-3* mutants (Fig. 5, A and B). However, the evoked EPSCs in *snt-1* mutants displayed a more severe reduction in 0.5 mM Ca²⁺ (a reduction in EPSC amplitude and charge transfer of ~85%; Fig. 5, A–C), indicating that SV fusion mediated by SNT-3 was more sensitive to a reduction in external Ca²⁺ with a decreased Ca²⁺ dependence.

The more reduction in lower Ca²⁺ and prolonged latency of the evoked EPSCs, together with the relatively diffuse axonal expression of SNT-3::mApple (Fig. 2), suggest that the SV release mediated by SNT-3 might occur further away from Ca²⁺ channels. This is supported by the accumulation of distally docked SVs in *snt-3* mutants. It is therefore likely that SNT-3 serves as a Ca²⁺ sensor for SV release that has loose coupling with Ca²⁺ entry. We have previously demonstrated that evoked neurotransmitter release at the worm NMJ consists of a fast component and a slow component, which reflect the release of SVs that have tight or loose coupling to Ca²⁺ entry and are mediated by the long and short isoforms of UNC-13, UNC-13L, and UNC-13MR (also called UNC-13S), respectively (Hu et al., 2013). Evoked EPSCs rescued by UNC-13L exhibited faster rise time and decay, as well as shorter latency, whereas evoked EPSCs rescued by UNC-13MR exhibited slower rise time and decay and prolonged latency, consistent with previous results (Fig. 5 E; Hu et al., 2013). To examine the involvement of SNT-3 in fast and slow SV release, we analyzed the effects of *snt-3* knockout in *unc-13* mutants expressing either UNC-13L or UNC-13MR (UNC-13L;*snt-3*, UNC-13MR;*snt-3*). The evoked EPSCs in UNC-13L;*snt-3* worms were indistinguishable from those in the UNC-13L rescued animals, indicating that SNT-3 is not required for UNC-13L-mediated fast release (Fig. 5, D and F); however, the evoked EPSCs in UNC-13MR;*snt-3* worms were dramatically reduced compared with those in UNC-13MR rescued animals (Fig. 5, D and F). These results reveal that SNT-3 serves as a

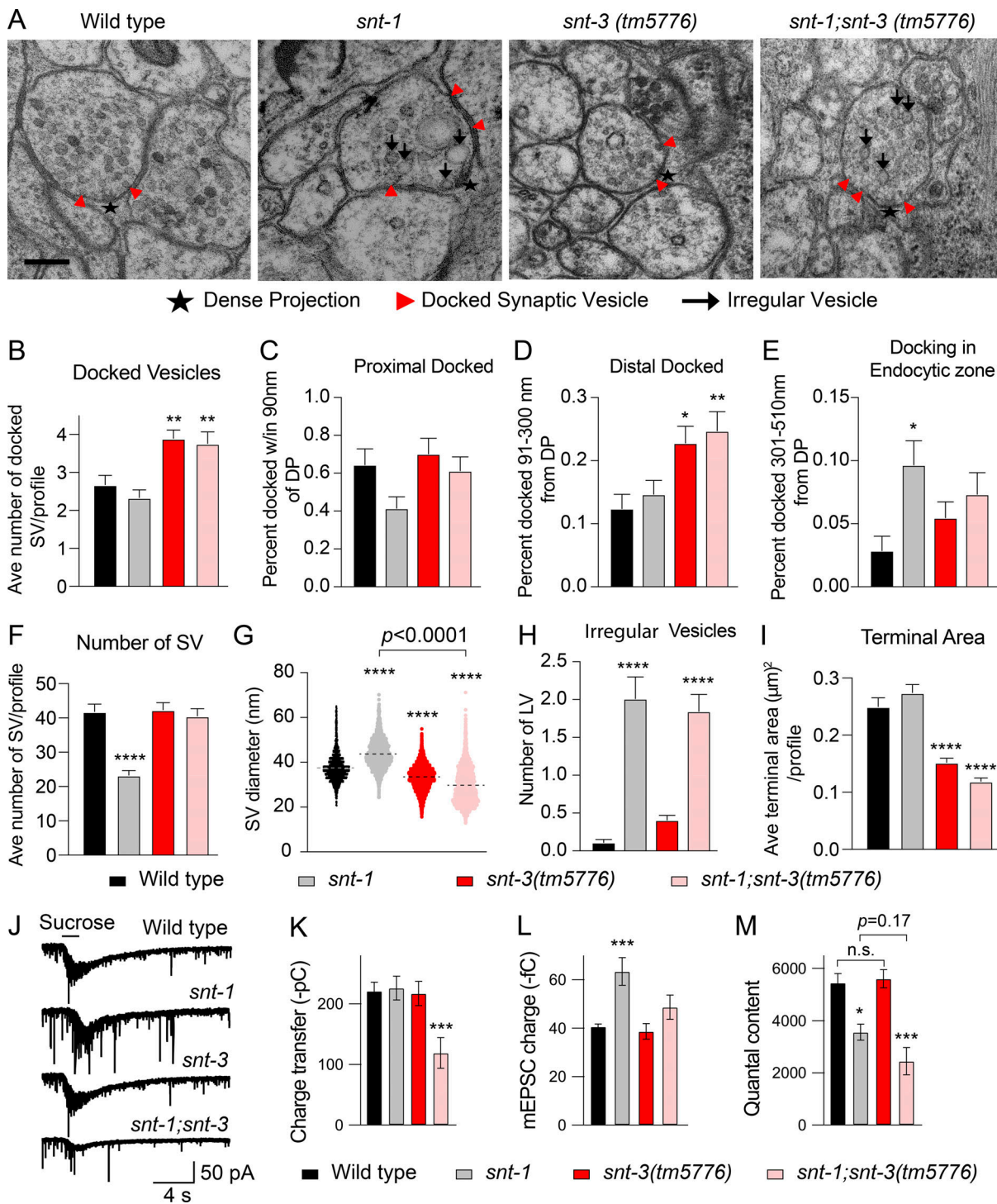


Figure 4. Roles of SNT-3 in SV docking and priming. (A) Representative synaptic profiles of the indicated genotypes, including WT, *snt-1* mutant, *snt-3* mutant, and *snt-1;snt-3* double mutant. Arrowhead indicates docked vesicles; star indicates DP, arrow indicates irregular vesicles. Scale bar, 200nm. (B-E) Quantification of docked SVs, docked within 90 nm of DP, docked between 91 and 300 nm from the DP, and docked between 301 and 510 nm from the DP from same genotypes as in A. The number of SVs docked at the plasma membrane was significantly increased in *snt-3* mutants and *snt-1;snt-3* double mutants, but unchanged in *snt-1* mutants. The number of SVs docked within 90 nm of the DP was reduced, though not to significance, in *snt-1* mutants, but unchanged in *snt-3* mutants and *snt-1;snt-3* double mutants. There was a significant increase in SVs docked between 91 and 300 nm from the DP in both *snt-3* mutants and *snt-1;snt-3* double mutants. Vesicles docked between 301 and 510 nm from the DP were significantly increased in *snt-1* mutants, with no change in *snt-3* mutants or *snt-1;snt-3* double mutants. Data are mean \pm SEM. * $P < 0.05$; ** $P < 0.01$ compared with WT (one-way ANOVA). (F-I) Quantification of total SV numbers, diameter of SVs (nm), number of irregular vesicles, and size of the terminal area (μm^2) from the same genotypes as in A. The total number of SVs was significantly decreased in *snt-1* mutants, with no change in *snt-3* mutants and *snt-1;snt-3* double mutants. The vesicle diameter was significantly increased in *snt-1* mutants, but significantly decreased in the *snt-3* mutant and *snt-1;snt-3* double mutants. There was an increase in the number of irregular vesicles in *snt-1* mutants and *snt-1;snt-3* double mutants, but no significant change in *snt-3* mutants. The terminal area was significantly reduced in the *snt-3* mutants and *snt-1*;

snt-3 double mutants, with no change in *snt-1* mutants. Data are mean \pm SEM. **** $P < 0.0001$ compared with WT (one-way ANOVA). **(J)** Hypertonic sucrose-evoked current recorded from WT, *snt-1* mutants, *snt-3* mutants, and *snt-1;snt-3* double mutants. **(K–M)** Quantification of averaged charge transfer in the sucrose-evoked currents, averaged mEPSC charge, and quantal content from the indicated genotypes. Data are mean \pm SEM. * $P < 0.05$, *** $P < 0.001$ compared with WT. n.s., nonsignificant (one-way ANOVA following Kruskal-Wallis test).

Ca^{2+} sensor specifically for SVs that have loose coupling to Ca^{2+} entry. Knockout of SNT-3 did not produce changes in mEPSC frequency in UNC-13L or UNC-13MR rescued animals, confirming that SNT-3 is not required for tonic release (Fig. 5, G and H).

SV release mediated by SNT-3 exhibits faster depression and slower replenishment

C. elegans cholinergic motor neurons stimulated by a train of depolarizations exhibit synaptic depression (Liu et al., 2009b; Schuske et al., 2003). The differences in Ca^{2+} sensitivity and Ca^{2+} coupling observed between SNT-1- and SNT-3-mediated SV release raised the question of how these two Ca^{2+} sensors regulate synaptic depression. To investigate this, a line expressing channelrhodopsin (*zxIs6*) was crossed into *snt-1* and *snt-3* mutants (*zxIs6;snt-1*, *zxIs6;snt-3*). The application of a 1-Hz or 5-Hz light train stimulus led to synaptic depression in control animals (i.e., *zxIs6*). Compared with control worms, synaptic depression was exacerbated in *snt-1* mutants, with significantly faster depression τ (Fig. 6, B and E); however, the depression τ was unchanged in *snt-3* mutants (Fig. 6, H and K), demonstrating that SNT-1 and SNT-3 have distinct roles in synaptic depression.

Faster depression in *snt-1* mutants may arise from a slower replenishment rate of SVs in the vesicular pool. When the replenishment rate was described by the slope of the cumulative EPSCs and calculated by a line fit through the linear section, we found that it was dramatically reduced in *snt-1* mutants under a 1-Hz or 5-Hz stimulus (Fig. 6, C and F), but was unchanged in *snt-3* mutants (Fig. 6, I and L). This indicates that the SV release mediated by SNT-3 has faster depression and slower replenishment, likely due to endocytic defects in the absence of SNT-1, which leads to a decrease in the total number of SVs as well as recycling rates (Fig. 4). Taken together, our data show that SNT-1 and SNT-3 trigger SV release with differential synaptic properties, including release kinetics, Ca^{2+} sensitivity, coupling to Ca^{2+} entry, and synaptic depression.

SNT-3 is activated when SNT-1 binding of Ca^{2+} is impaired

How are the two Ca^{2+} sensors coordinated in neurons? The WT evoked EPSCs in *snt-3* mutants versus the elimination of evoked EPSCs in *snt-1;snt-3* double mutants indicate that SNT-3 is inactive when SNT-1 is present, but activated when SNT-1 is ablated. It therefore appears that SNT-3 activity is suppressed by SNT-1 under physiological conditions. Several possibilities may account for the functional activation of SNT-3. First, the abundance of SNT-3 may be increased in the absence of SNT-1. To test this possibility, we examined the expression level of SNT-3 in *snt-1* mutants. As shown in Fig. 7 (A and B), the fluorescence intensity of SNT-3::mApple in *snt-1* mutants was indistinguishable from that in WT animals, indicating that SNT-1 does not

suppress the expression of SNT-3. Hence, the activation of SNT-3 in *snt-1* mutants is not due to a change in its synaptic abundance.

Second, Ca^{2+} that flows into the nerve terminals in response to stimulation could be strongly buffered by SNT-1, resulting in a rapid decrease in the Ca^{2+} concentration in the Ca^{2+} microdomain. Consequently, SNT-3 would be less competitive in binding Ca^{2+} and could not be activated in the presence of SNT-1. If this were the case, we would expect that SNT-3 could be activated by diminishing or abolishing the Ca^{2+} -binding ability of SNT-1. To test this, we examined the effects of reducing SNT-1 Ca^{2+} binding on SNT-3 function by mutating the third and fourth Ca^{2+} -binding sites (aspartate to asparagine, D to N) in the C2A, C2B, or C2A and C2B domains in SNT-1—termed SNT-1^{C2A D3,4N}, SNT-1^{C2B D3,4N}, and SNT-1^{C2AB D3,4N}. We have previously demonstrated that the D3,4N mutations in the C2 domains of SNT-1 completely abolish its Ca^{2+} -binding ability (Li et al., 2018). Evoked EPSCs were completely restored by the pan-neuronal expression of WT SNT-1 in *snt-1* mutants (SNT-1^{C2AB}; *snt-1*; Fig. 7, C and D). As expected, knockout of *snt-3* in SNT-1^{C2AB}-rescued worms did not cause a change in evoked EPSCs; however, *snt-3* knockout resulted in a pronounced decrease in evoked EPSCs when Ca^{2+} binding was disrupted in either the C2A or C2B domain in SNT-1 (SNT-1^{C2A D3,4N}; *snt-1;snt-3*, SNT-1^{C2B D3,4N}; *snt-1;snt-3*), and complete elimination of evoked EPSCs when Ca^{2+} binding was blocked in both C2 domains (SNT-1^{C2AB D3,4N}; *snt-1;snt-3*; Fig. 7, C and D). In contrast, neuronal expression of SNT-3 restored evoked release in SNT-1^{C2AB D3,4N}; *snt-1;snt-3* to *snt-1* single mutant levels. These results indicate that SNT-3 is activated and able to trigger SV fusion when SNT-1 binding of Ca^{2+} is impaired, likely due to the ability of this Ca^{2+} sensor to bind Ca^{2+} effectively.

We next examined whether the elimination of the evoked EPSCs in SNT-1^{C2AB D3,4N}; *snt-1;snt-3* animals arises from a priming defect. The sucrose-evoked charge transfer and quantal content were not changed by mutating the Ca^{2+} -binding sites in the C2A or C2B domains in SNT-1, but were significantly decreased by mutating these sites in both domains simultaneously (Fig. 7, F and G), demonstrating that the role of SNT-1 in priming requires Ca^{2+} binding by at least one of its C2 domains. Although the evoked EPSCs were largely decreased in SNT-1^{C2A D3,4N}; *snt-1;snt-3* and SNT-1^{C2B D3,4N}; *snt-1;snt-3* animals, the sucrose-evoked charge transfer and quantal content were normal in these animals (Fig. 7, F and G), demonstrating a postpriming role for SNT-3 in triggering fusion when SNT-1 binding of Ca^{2+} is impaired. However, the sucrose-evoked charge transfer and quantal content were slightly but significantly reduced (~30%) in SNT-1^{C2AB D3,4N}; *snt-1;snt-3* animals (Fig. 7, F and G), indicating that SNT-3 plays a minor role in priming when SNT-1 binding of Ca^{2+} is abolished. This minor decrease in priming, however, could not account for the elimination of the evoked EPSCs in SNT-1^{C2AB D3,4N}; *snt-1;snt-3* animals, confirming the postpriming role of

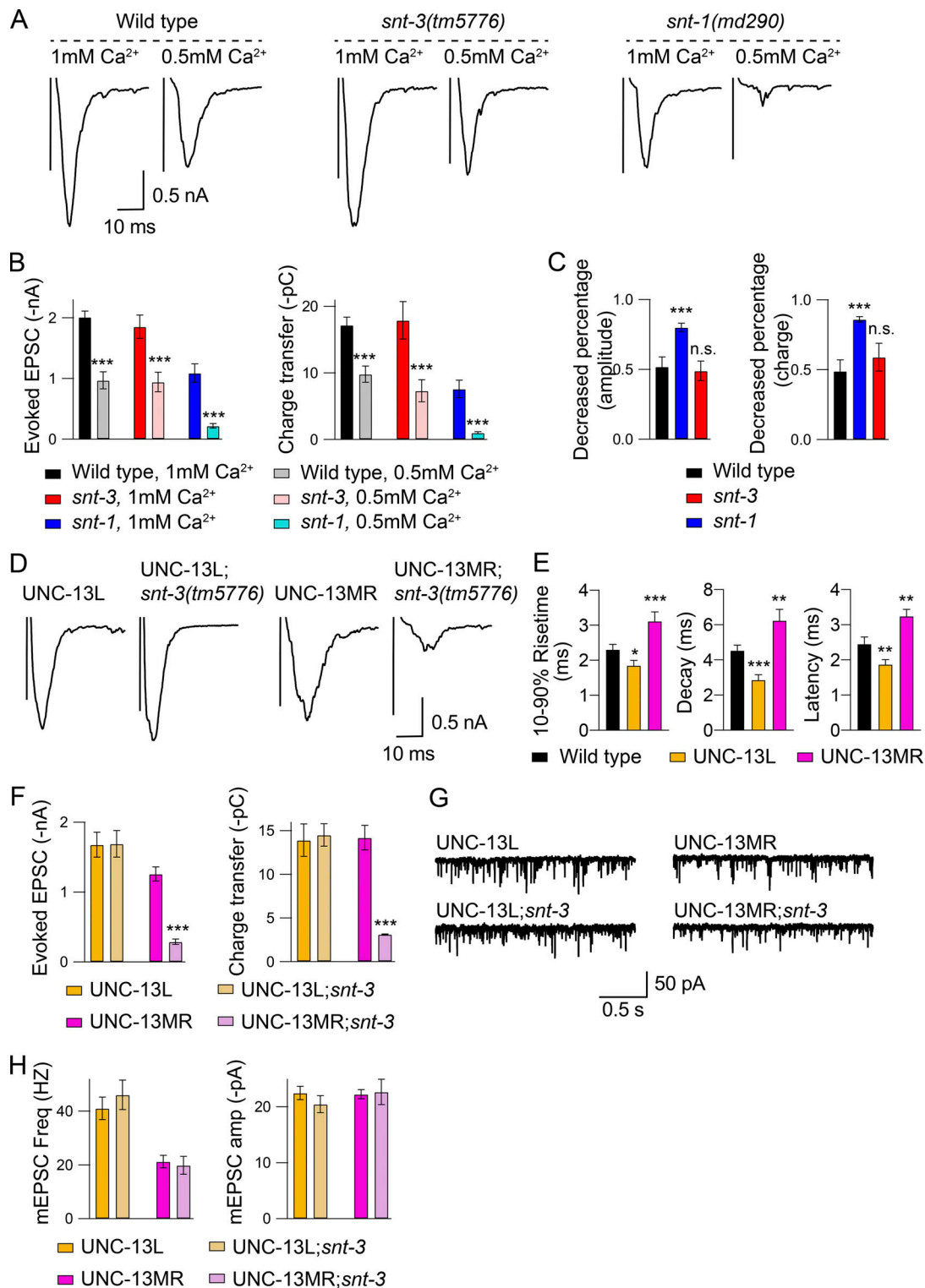


Figure 5. SNT-3 triggers release of SVs that have loose coupling with Ca²⁺ entry. (A) Representative traces of evoked EPSCs from WT, *snt-1*, and *snt-3* mutants in 1 mM and 0.5 mM Ca²⁺. (B) Summary of the mean amplitude and charge transfer of evoked EPSCs in A. Data are mean ± SEM. ***P < 0.001 compared with the same genotype in 1 mM Ca²⁺ (Student's *t* test). (C) Decreased percentage of evoked EPSC amplitude and charge transfer in 0.5 mM Ca²⁺ compared with that in 1 mM Ca²⁺ from the indicated genotypes. Data are mean ± SEM. ***P < 0.001 compared with WT. n.s., nonsignificant compared with WT (one-way ANOVA). (D and G) Example traces of mEPSCs and evoked EPSCs from the indicated genotypes, including UNC-13L rescue, UNC-13L;*snt-3*, UNC-13MR rescue, and UNC-13MR;*snt-3*. (E) Averaged 10% to 90% rise time, inactivation decay, and latency from evoked EPSCs in UNC-13L and UNC-13MR rescued animals. Data are mean ± SEM. *P < 0.05; **P < 0.01; ***P < 0.001 compared with WT (one-way ANOVA). (F and H) Quantification of evoked EPSC amplitude and charge transfer, and mEPSC frequency and amplitude from the same genotypes in D and F. Data are mean ± SEM. ***P < 0.001 compared with UNC-13MR rescue (one-way ANOVA).

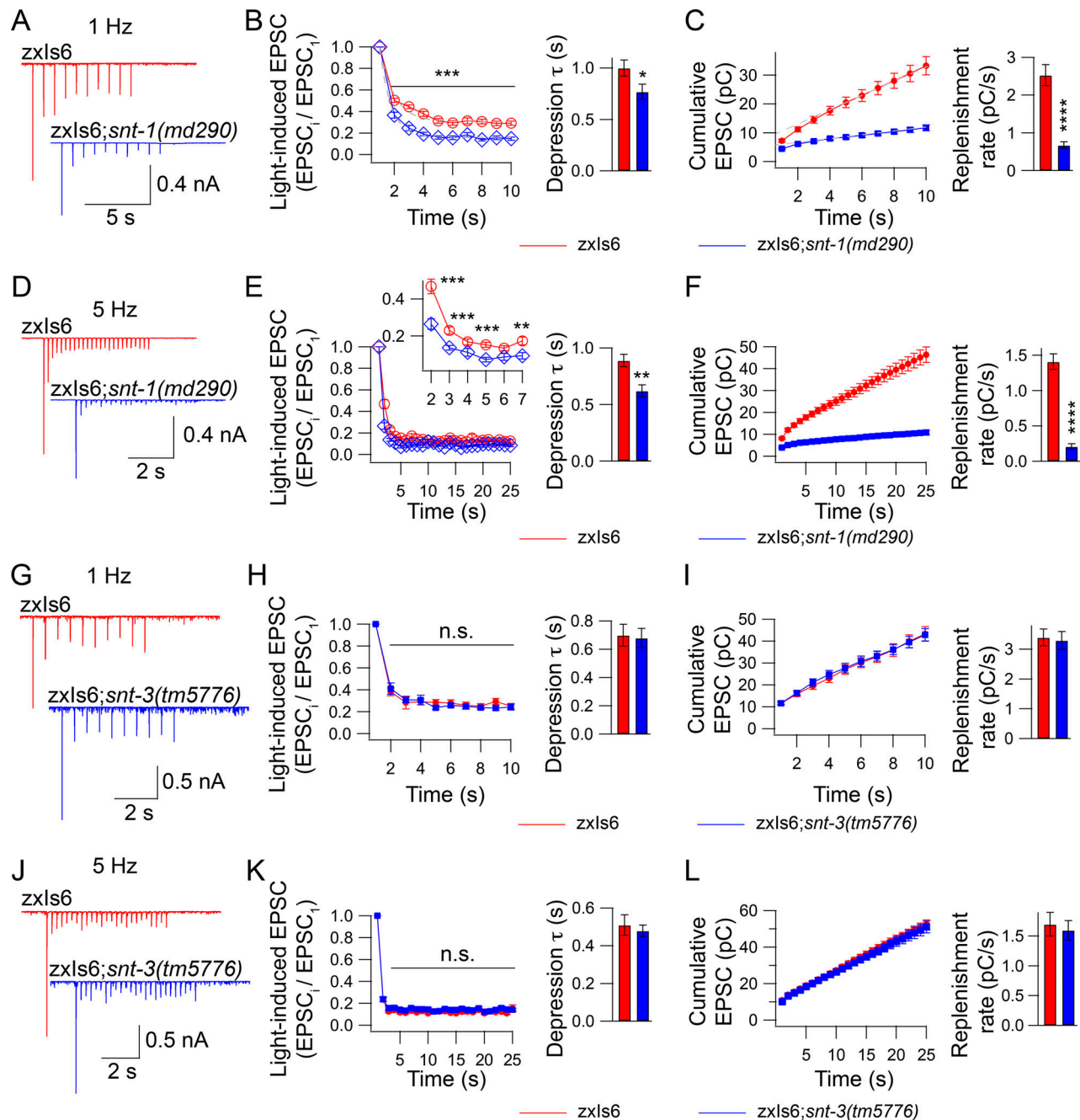


Figure 6. SNT-1 and SNT-3 have differential roles in synaptic depression and replenishment. Synaptic depression and SV replenishment were investigated by applying a train light stimulus (1 Hz and 5 Hz) onto the ventral nerve cord of control animals (*zxls6*) and *snt-1(md290)* and *snt-3(tm5776)* mutants with expression of Chr2 in their cholinergic motor neurons. **(A, D, G, and J)** Example traces of 1-Hz and 5-Hz light train stimulus-evoked EPSCs from *zxls6* (red), *zxls6;snt-1* (blue), and *zxls6;snt-3* (blue) animals. **(B, E, H, and K)** Quantification of synaptic depression by normalizing the EPSC amplitude (EPSC_i) to the first EPSC amplitude (EPSC₁), and depression τ of the normalized EPSC amplitude (calculated by fitting the normalized depression curve using monoexponential function; dashed gray curve). Data are mean \pm SEM. n.s., nonsignificant. **P* < 0.05; ***P* < 0.01; ****P* < 0.001 compared with *zxls6* (Mann-Whitney test). **(C, F, I, and L)** Averaged cumulative EPSC amplitudes during 1-Hz and 5-Hz trains, and quantification of the replenishment rate. Replenishment rate was described by the slope of the cumulative EPSCs and calculated by a line fit through the linear section (dashed gray line). Data are mean \pm SEM. *****P* < 0.0001 compared with *zxls6* (Student's *t* test).

SNT-3 in SV fusion. These results are consistent with earlier findings in *snt-1;snt-3* double mutants (Fig. 4 M).

Unlike its effects on evoked EPSCs, the loss of SNT-3 did not cause changes in mEPSCs when SNT-1 binding of Ca²⁺ was impaired. Of note, mEPSC frequency was reduced by 50% when

Ca²⁺ binding in SNT-1 was abolished (i.e., SNT-1^{C2AB D3,4N}; Liu et al., 2018). Despite this, there was no further decrease in SNT-1^{C2AB D3,4N}; *snt-1;snt-3* mutants (Fig. 7, H and I). These results, together with the observations in *snt-1;snt-3* double mutants, demonstrate that SNT-3 is unable to trigger tonic release. The

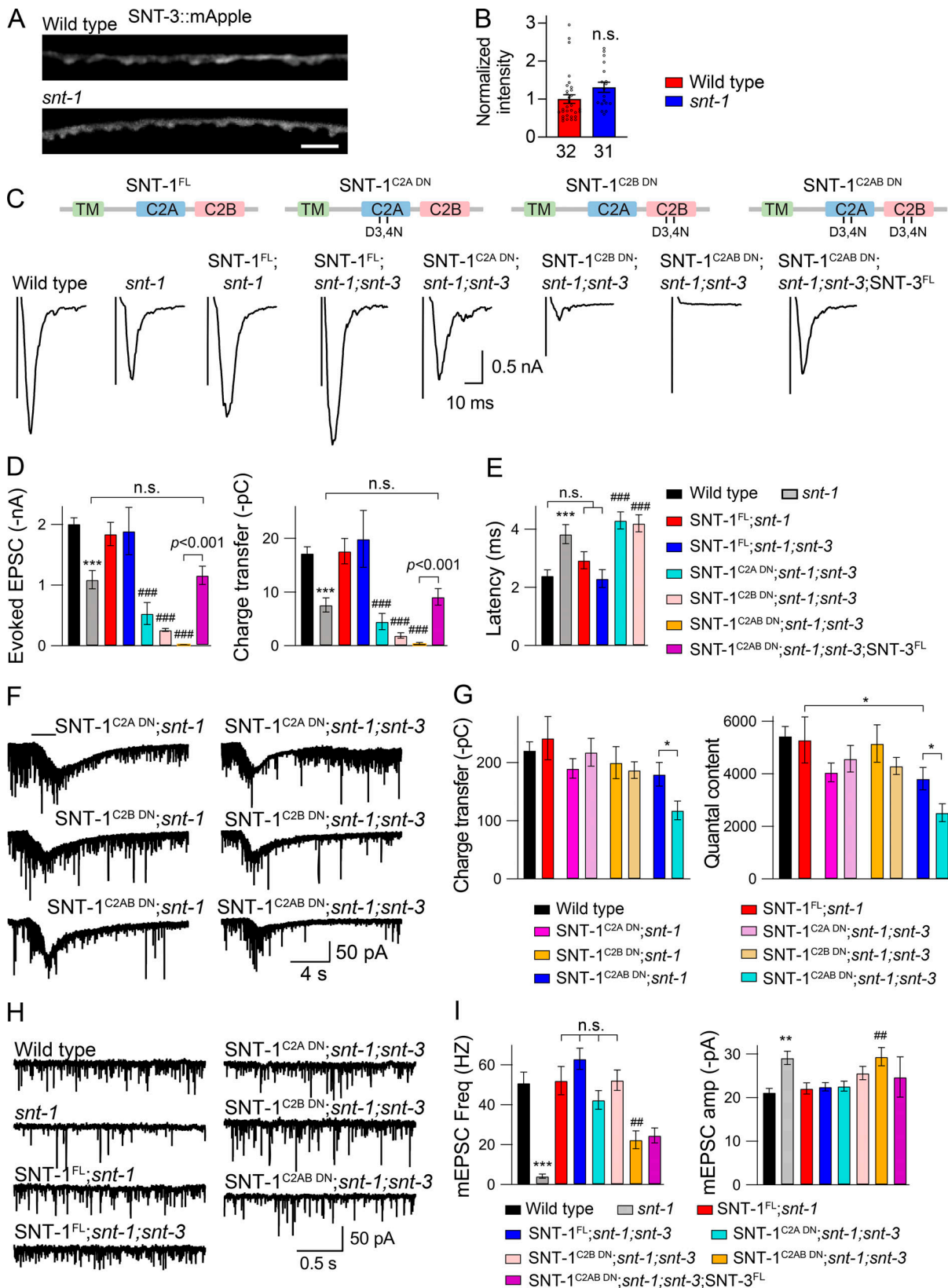


Figure 7. **SNT-3 triggers a delayed release when SNT-1 binding Ca^{2+} is impaired.** (A) Representative images showing the SNT-3::mApple distribution in cholinergic axons in WT and *snt-1* mutant background. Scale bar, 5 μ m. (B) Quantification of fluorescence intensity of SNT-3::mApple. Data are mean \pm SEM. n.s., nonsignificant (Student's *t* test). (C–E) Example traces of evoked EPSCs and summary of the EPSC amplitude, charge transfer, and latency. Data are mean \pm SEM. ****P* < 0.001 compared with WT; ###*P* < 0.001 compared with SNT-1^{C2A DN}; *snt-1*; *snt-3* transgenes. n.s., nonsignificant (one-way ANOVA). (F and G) Example traces of hypertonic sucrose-evoked currents, and quantification of charge transfer and quantal content of the sucrose-evoked currents. Data are

mean \pm SEM. * $P < 0.05$ (one-way ANOVA). **(H and I)** Representative mEPSC traces and summary of mEPSC frequency and amplitude from the indicated genotypes and transgenes. Data are mean \pm SEM. ** $P < 0.01$, *** $P < 0.001$ compared with WT; ## $P < 0.01$ compared with SNT-1^{C2AB D3,4N};snt-1;snt-3 transgenes. n.s., nonsignificant (one-way ANOVA following Kruskal-Wallis test).

increase in mEPSC amplitude when Ca²⁺ binding in SNT-1 was abolished is similar to that of *snt-1*-null mutants, suggesting that the endocytic role of SNT-1 mutants requires Ca²⁺ binding.

Ca²⁺ binding to the C2B domain of SNT-3 is essential for SV release

Given the Ca²⁺-binding properties and the conserved Ca²⁺-binding sites in the C2 domain of SNT-3, we next examined the impact of C2A versus C2B mutations on SNT-3 function. SNT-3 rescue constructs carrying mutations of the third and fourth Ca²⁺-binding sites (aspartate to asparagine, D to N) in the C2A or C2B domains (SNT-3^{C2A D3,4N}, SNT-3^{C2B D3,4N}) were constructed and expressed in *snt-1*;*snt-3* double mutants (Fig. 8 A). Compared with the WT SNT-3 rescue (SNT-3^{C2AB}), Ca²⁺ binding to the C2A domain did not cause a change in evoked EPSCs, whereas disrupting Ca²⁺ binding to the C2B domain completely eliminated evoked slow EPSCs (Fig. 8, B and C). These results demonstrate that the role of SNT-3 in triggering Ca²⁺-dependent release is predominately determined by the C2B domain binding of Ca²⁺, differing from the mouse slow Ca²⁺ sensor, Syt7, which triggers slow asynchronous release through its C2A domain (Bacaj et al., 2013).

As SNT-3 is not required for tonic release (Fig. 1 and Fig. 7), it is unlikely that the Ca²⁺-binding mutations in SNT-3 would cause changes in mEPSC frequency. Compared with the WT SNT-3 rescue in *snt-1*;*snt-3* double mutants, Ca²⁺-binding mutations in the C2A domain (SNT-3^{C2A D3,4N};snt-1;snt-3) did not alter mEPSC frequency; however, Ca²⁺-binding mutations in the C2B domain (SNT-3^{C2B D3,4N};snt-1;snt-3) caused a significant decrease in mEPSC frequency (6.4 \pm 2.4 Hz vs. 1.7 \pm 0.9 Hz; Fig. 8, D and E), probably due to the fact that the C2B DN mutations produced an even stronger defect in endocytosis than *snt-1* mutants based on the increase in mEPSC amplitude. In fact, it has been reported that, at the fly NMJ, C2B DN mutations in Syt1 caused an even stronger decrease in neurotransmitter release than that in Syt1-null mutants (Mackler et al., 2002). Moreover, the mEPSC amplitude was increased by the overexpression of WT or mutated SNT-3 in *snt-1*;*snt-3* double mutants (Fig. 8 and Fig. S7). Given that the vesicle size was decreased in *snt-3* mutants (Fig. 4), this may represent an opposing effect in vesicle recycling induced by overexpression of SNT-3.

Cytoplasmic SNT-1 is functional and triggers fast release

Given the distinct N termini of SNT-3 and SNT-1, we wondered if this region accounts for the differences in their release properties. To address this question, we made SNT-1 rescue constructs deleting either the TM domain (70–96 aa; SNT-1 ^{Δ TM}) or the whole N terminus (0–155 aa; SNT-1 ^{Δ N}; Fig. 9 A). We found that the expression levels of SNT-1 ^{Δ TM}::mApple and SNT-1 ^{Δ N}::mApple in cell bodies were comparable between WT and *unc-104* mutants (data not shown), unlike the SNT-1::mApple, which exhibited increased fluorescence in cell bodies in the *unc-104*

mutant background (Fig. 2 H). This indicates that SNT-1 is not targeted to SVs when the TM domain is removed.

Despite the loss of SV association, both SNT-1 ^{Δ TM}::mApple and SNT-1 ^{Δ N}::mApple exhibited similar distributions to SNT-1::mApple in cholinergic synapses, as well as good colocalization with UNC-10::GFP (Fig. 9 B), indicating that the synaptic localization of SNT-1 is not determined by its N-terminal-mediated membrane tethering. Instead, its C2 domains appear to be sufficient to promote targeting at active zones. To confirm this, we examined the distribution of the individual C2A and C2B domains. Our results showed that both C2A::mApple and C2B::mApple displayed good colocalization with UNC-10::GFP (Fig. S8), demonstrating the important roles of C2 domains in localizing SNT-1, likely by interacting with the SNARE complex and the plasma membrane.

We then examined whether cytoplasmic SNT-1 is functional. The *snt-1* mutants rescued by neuronal expression of SNT-1 ^{Δ TM} or SNT-1 ^{Δ N} exhibited significantly better movement than *snt-1* mutant worms, with locomotion speed being restored to an almost WT level (\sim 85% of WT; Fig. 9, C and D), demonstrating that cytoplasmic SNT-1 was still functional in the nervous system. The body length of the *snt-1* mutant worms was significantly rescued by SNT-1 ^{Δ TM} or SNT-1 ^{Δ N} (Fig. S9). Moreover, the SNT-1 ^{Δ TM} and SNT-1 ^{Δ N} rescued worms displayed smooth backward movement compared with *snt-1* mutants, which exhibited jerky, uncoordinated backward locomotion (data not shown). Consistent with the locomotion results, evoked EPSCs were partially restored by SNT-1 ^{Δ TM} or SNT-1 ^{Δ N}, as demonstrated by recordings in both 1 mM Ca²⁺ and 0.5 mM Ca²⁺ (Fig. 9, E–H). The evoked EPSC rise time, latency, and amplitude were nearly indistinguishable from those rescued by full-length SNT-1 (SNT-1^{C2AB}, in 1 mM Ca²⁺), although the EPSC decay in SNT-1 ^{Δ TM} and SNT-1 ^{Δ N} rescued animals was significantly faster than that observed in the SNT-1^{C2AB} rescued animals, leading to a decreased charge transfer (Fig. 9 H). The faster decay of the evoked EPSCs did not arise from a change in the inactivation of postsynaptic AChRs, as the decay of the averaged mEPSCs was unaltered in SNT-1 ^{Δ TM} and SNT-1 ^{Δ N} rescued animals (Fig. S10, A and B). Although it is still unclear how deleting the TM domain results in faster decay, our results demonstrate that cytoplasmic SNT-1 is still able to trigger fast neurotransmitter release.

Despite the fast release kinetics observed in SNT-1 ^{Δ TM} and SNT-1 ^{Δ N} rescued animals, the evoked EPSC amplitudes in these animals were significantly lower than those in the full-length SNT-1 rescued animals in 0.5 mM Ca²⁺ (Fig. 9, F–H), suggesting that SNT-1–SV tethering determines the amount of neurotransmitter release, perhaps due to looser coupling between docked SVs and Ca²⁺ entry. Decreasing the Ca²⁺ concentration from 1 mM to 0.5 mM led to similar reductions in evoked charge transfer in WT (51%), SNT-1 ^{Δ TM} rescued worms (60%), and SNT-1 ^{Δ N} rescued worms (56%), indicating that disrupting SNT-1–SV tethering does not affect the Ca²⁺ dependence of SV release (data

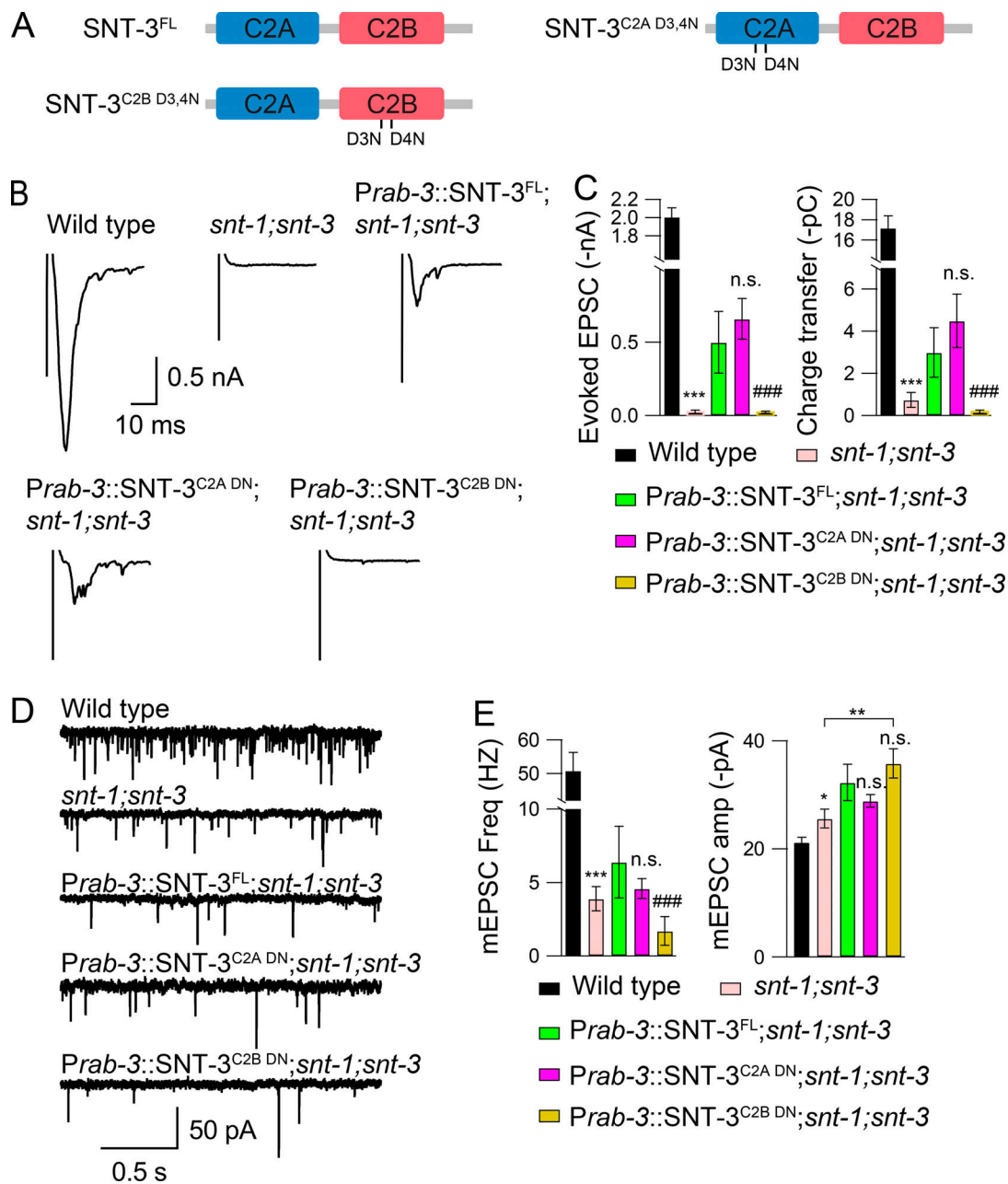


Figure 8. Ca²⁺ binding by the C2B domain in SNT-3 triggers delayed evoked neurotransmitter release. (A) WT (SNT-3^{FL}) and mutated SNT-3 rescue constructs containing Ca²⁺-binding mutations in the C2A or C2B domains (SNT-3^{C2A DN}, SNT-3^{C2B DN}). (B and C) Representative traces of evoked EPSCs, and quantification of the EPSC amplitude and charge transfer from the indicated genotypes and transgenes. Disrupting Ca²⁺ binding in the C2B domain, but not the C2A domain, in SNT-3 blocked SNT-3-mediated evoked EPSCs. Data are mean ± SEM. **P < 0.01, ***P < 0.001 compared with WT; ###P < 0.001 compared with SNT-3^{C2AB};snt-1;snt-3 transgenes. n.s., nonsignificant compared with SNT-3^{C2AB};snt-1;snt-3 transgenes (one-way ANOVA). (D and E) Example mEPSC traces and averaged mEPSC frequency and amplitude from the indicated genotypes and transgenes. Data are mean ± SEM. **P < 0.05, ***P < 0.001 compared with WT; *P < 0.01 compared to *snt-1;snt-3* double mutants; ###P < 0.001 compared with SNT-3^{C2AB};snt-1;snt-3 transgenes. n.s., nonsignificant compared with SNT-3^{C2AB};snt-1;snt-3 transgenes (one-way ANOVA).

not shown). We next examined whether SNT-1-SV tethering is required for priming. Our data revealed that both the sucrose-evoked charge transfer and quantal content were unchanged in SNT-1^{ΔTM} and SNT-1^{ΔN} rescued animals compared with full-length SNT-1 rescue animals (Fig. 9, I and J), indicating that the SNT-1-SV tethering is not necessary for priming. Consequently, the probability of neurotransmitter release (P_{vr}),

calculated by the ratio of the evoked charge transfer to the total charge transfer in the RRP (Gerber et al., 2008; Li et al., 2019), was markedly decreased by disrupting SNT-1-SV tethering (Fig. 9 K).

Consistent with our evoked EPSC results, the mEPSC frequency was rescued by 50% of that observed in SNT-1C2AB rescue by SNT-1^{ΔTM} and SNT-1^{ΔN} in *snt-1* mutants in both 1 mM

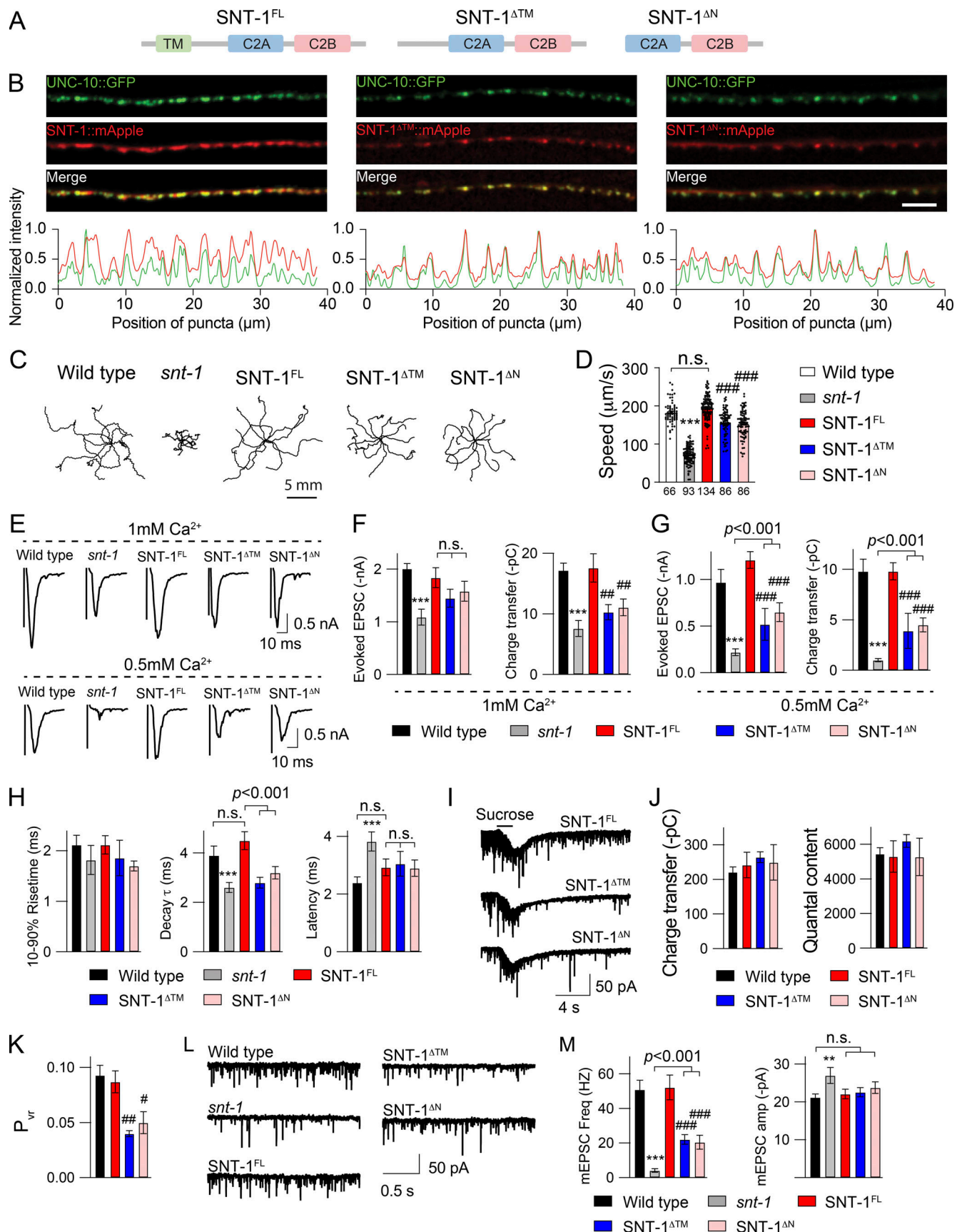


Figure 9. **Cytoplasmic SNT-1 supports locomotion and triggers fast neurotransmitter release.** (A) Generation of cytoplasmic SNT-1 rescue constructs (SNT-1^{ΔTM} and SNT-1^{ΔN}). (B) Synaptic localization of SNT-1::mApple, SNT-1^{ΔTM}::mApple, and SNT-1^{ΔN}::mApple in cholinergic axons (under the *unc-129*

promoter). Both cytoplasmic SNT-1 constructs display similar distribution with the full-length SNT-1 and exhibit well colocalization with the active zone marker UNC-10::GFP. **(C and D)** Representative locomotory trajectories and quantification of the average locomotion speed for the indicated genotypes, including WT, *snt-1*, full-length SNT-1 rescue, and cytoplasmic SNT-1 rescue (SNT-1^{ΔTM} and SNT-1^{ΔN}) in *snt-1* mutants. Data are mean ± SEM. ***P < 0.001 compared with WT; ###P < 0.001 compared with *snt-1* mutants. n.s., nonsignificant (one-way ANOVA). **(E–H)** Example traces of evoked EPSCs recorded in both 1 mM and 0.5 mM Ca²⁺ solution, and quantification of the EPSC amplitude, charge transfer, and latency from the same genotypes and transgenes in C. Data are mean ± SEM. ***P < 0.001 compared with WT; ##P < 0.01, ###P < 0.001 compared with full-length SNT-1 rescue. n.s., nonsignificant (one-way ANOVA). **(I and J)** Example traces of hypertonic sucrose-evoked currents, and quantification of charge transfer and quantal content from *snt-1* mutants rescued by full-length or cytoplasmic SNT-1. Data are mean ± SEM. **(K)** Quantification of the release probability (P_{vr}). Data are mean ± SEM. #P < 0.05; ##P < 0.01 compared with full-length SNT-1 rescue (one-way ANOVA). **(L and M)** Example mEPSC traces and averaged mEPSC frequency and amplitude from the indicated genotypes and transgenes. Data are mean ± SEM. **P < 0.01; ***P < 0.001 compared with WT; ###P < 0.001 compared with full-length SNT-1 rescue. n.s., nonsignificant (one-way ANOVA).

Ca²⁺ and 0.5 mM Ca²⁺, with the mEPSC amplitude and charge being nearly completely rescued (Fig. 9, L and M; Fig. S9 C; and Table S1). This indicates that cytoplasmic SNT-1 is also capable of triggering tonic release. Taken together, our results demonstrate that cytoplasmic SNT-1 is still capable of supporting locomotory behavior and triggering fast Ca²⁺-dependent neurotransmitter release, but that SNT-1–SV untethering negatively impacts release probability. Moreover, these data suggest that the distinct release properties of SNT-1 and SNT-3 arise from their intrinsically different C2 domains.

Discussion

Of the 17 identified mammalian Syt isoforms, several are known to act as Ca²⁺ sensors used to trigger Ca²⁺-dependent neurotransmitter release, including Syt1, Syt2, Syt7, and Syt9 (Geppert et al., 1994; Lee et al., 2013; Littleton et al., 1993; Luo et al., 2015; Stevens and Sullivan, 2003; Weber et al., 2014; Xu et al., 2007). Of the seven known Syts in *C. elegans*, only SNT-1 has been shown to act as a Ca²⁺ sensor for neurotransmitter release. A behavioral and electrophysiological screen of the remaining Syt genes in *C. elegans* identified a new Ca²⁺ sensor, SNT-3, which is required for delayed neurotransmitter release. Unlike other known Ca²⁺ sensors in the Syt family, SNT-3 has a truncated N terminus that lacks a TM domain. Despite this structural difference, our results demonstrate that this short Syt isoform plays essential roles in the nervous system and triggers delayed Ca²⁺-dependent neurotransmitter release in the absence of SNT-1, the fast Ca²⁺ sensor in *C. elegans*. Thus, our findings provide significant insights into the molecular mechanisms whereby Ca²⁺ sensors regulate fast and slow neurotransmitter release.

The dual Ca²⁺ sensor model for Ca²⁺-dependent neurotransmitter release

A dual Ca²⁺ sensor system has been found in many neuronal types, such as hippocampal and cortical neurons in mouse and motor neurons in zebrafish, in which either Syt1 or Syt2 is employed as the fast Ca²⁺ sensor to trigger fast synchronous release, and Syt7 is employed as the slow Ca²⁺ sensor to trigger slow asynchronous release. Our findings reveal an alternative dual Ca²⁺ sensor system at the worm NMJ, which uses SNT-1 and SNT-3 to trigger fast and delayed neurotransmitter release, thereby extending the two-Ca²⁺-sensor system to invertebrates. Although we cannot conclude that SNT-3 is a slow Ca²⁺ sensor like Syt7 due to the fast decay of the evoked EPSCs mediated by

SNT-3, these two Ca²⁺ sensors share many similarities, including localization and function. It should be noted that not all model organisms use a two-Ca²⁺-sensor system for SV exocytosis. One recent study showed that Syt7 negatively regulates SV release at the *Drosophila* NMJ, with Syt1/7 double mutants displaying more release than Syt1 mutants alone, suggesting that the two-Ca²⁺-sensor system of Syt1 and Syt7 is not applicable at *Drosophila* synapses (Guan et al., 2020).

The worm dual-Ca²⁺-sensor system has analogous features to those of mice in several respects. First, the two Ca²⁺ sensors are tethered on distinct cellular membranes. Both Syt-1 and SNT-1 have a conserved N-terminal TM domain, which tethers the proteins on SVs (Fig. 2; Brose et al., 1992; Li et al., 2018; Littleton et al., 1993). In contrast, the TM domain in Syt7 anchors it on the plasma membrane (Maximov et al., 2008; Sugita et al., 2001). In contrast to neuroendocrine cells, Syt7 is colocalized with Syt1 on secretory granules (Schonn et al., 2008; Wang et al., 2005). Moreover, Syt7 is localized to an internal membrane tubular network within the periaxial zone (Guan et al., 2020). Nevertheless, SNT-3 does not appear to be associated with SVs as it lacks a TM domain, does not undergo a change in expression pattern in *unc-13* mutants, and is not retained in the cell soma upon disruption of the SV kinesin motor protein, UNC-104 (Fig. 2). The C2 domains in SNT-3, however, do exhibit Ca²⁺-dependent membrane binding (Fig. 3), suggesting that this cytoplasmic Ca²⁺ sensor may interact with either the SV or plasma membrane once activated. Second, knockout of either of the two Ca²⁺ sensors produces similar effects on baseline neurotransmitter release. The fast evoked EPSCs are similarly reduced in mouse/fly Syt1 mutants and worm *snt-1* mutants (Lee et al., 2013; Li et al., 2018; Nishiki and Augustine, 2004; Xu et al., 2007; Yoshihara and Littleton, 2002) with prolonged latency. Whereas evoked EPSCs are unaltered in Syt7 knockout mice or *snt-3* mutant worms (Bacaj et al., 2013; Maximov et al., 2008; Weber et al., 2014), the effect of Syt7 or SNT-3 knockout on baseline evoked transmitter release is only observed in the absence of Syt1 or SNT-1 (Fig. 1), suggesting a common mechanism by which the primary Ca²⁺ sensor (Syt1 and SNT-1) suppresses the secondary Ca²⁺ sensor (Syt7 and SNT-3) under physiological conditions. Third, simultaneous loss of both Ca²⁺ sensors (i.e., Syt1/7 and SNT-1/3) reduces the size of the readily releasable vesicle pool to almost the same extent (Fig. 4), suggesting similar functions in regulating priming (Bacaj et al., 2015).

These similarities indicate that the dual-Ca²⁺-sensor system may operate via similar mechanisms in distinct model organisms.

It has been proposed that the slow Ca^{2+} sensor, Syt7, is somehow suppressed by the fast Ca^{2+} sensor, Syt1, based on the observation that the asynchronous release mediated by Syt7 is increased in Syt1 knockout neurons (Nishiki and Augustine, 2004; Yoshihara et al., 2010). Our data support this notion by showing that SNT-3 cannot be activated in the presence of SNT-1. One possible model for this suppression is that the local Ca^{2+} concentration decays rapidly due to the fast robust Ca^{2+} buffering of SNT-1, which prevents Ca^{2+} binding to SNT-3. This hypothesis is supported by our findings that SNT-3 can be activated when Ca^{2+} binding to SNT-1 is impaired (Fig. 7). In the mouse central nervous system, the contribution of Syt7 to transmitter release can also be observed by prolonging the duration of depolarization (Luo et al., 2015) or applying multiple stimuli (Jackman et al., 2016), all of which could elevate and prolong the local Ca^{2+} concentration allowing Syt7 activation.

Ca^{2+} sensors in docking and priming

Despite the functional importance and similarities of the fast Ca^{2+} sensor Syts in triggering fast synchronous release, their functions in SV priming remain controversial. The RRP is unaltered or decreased in Syt1 or Syt2 knockout neurons in cultured hippocampal or cortical neurons (Bacaj et al., 2015; Liu et al., 2009a; Pang et al., 2006), and it is almost abolished by the loss of Syt1 in the fly NMJ (Yoshihara et al., 2010). Although the total sucrose-evoked charge transfer was normal in *snt-1* mutants, the quantal content in the RRP was slightly but significantly reduced (30%; Fig. 4), indicating that SNT-1 plays a minor role in priming. Despite these inconsistent observations regarding fast Ca^{2+} sensors in priming, knockout of Syt7 or SNT-3 does not cause a priming defect due to compensation by Syt1 or SNT-1. This was confirmed by the substantial decrease in the sucrose-evoked charge transfer and quantal content in the *snt-1*; *snt-3* double mutants (Fig. 4) and in Syt1/7 double-knockout neurons (Bacaj et al., 2015). Our findings therefore support the notion that both Ca^{2+} sensors may contribute to SV priming (i.e., Syt1/7 and SNT-1/3).

SV docking has been shown to be normal in Syt1 knockout neurons in the mouse central nervous system (Geppert et al., 1994; Imig et al., 2014); however, the docking process is severely disrupted in fly Syt1 mutants, with the numbers of total and docked SVs largely reduced, which may underlie the profound decrease in the RRP at the fly NMJ (Lee et al., 2013; Reist et al., 1998). We found that the total number of SVs in synaptic terminals was decreased by 50% with the loss of SNT-1, which is consistent with previous findings supporting a role for SNT-1 in endocytosis (Jorgensen et al., 1995; Yu et al., 2013; Fig. 4). While the number of docked SVs was not significantly reduced in *snt-1* mutants, vesicles that were docked proximal to the DP were, indicating that SNT-1 may impact the stability of SV docking and contribute to the loss of fast synchronous release. The decreased total number of SVs in *snt-1* mutants due to endocytic defects may account for the slow replenishment rate of the vesicle pool following a train stimulus (Fig. 6).

Unexpectedly, we observed a decreased terminal area and increased number of docked SVs in *snt-3* mutants (Fig. 4), indicating that SNT-3 has additional unknown functions at the

synapse. Interestingly, the increase in docked SVs did not result in a larger RRP in *snt-3* mutants. One possibility is that SNT-3 is required for full zippering of the SNARE complex in the priming process, with some vesicles appearing docked but not fusion competent in *snt-3* mutants. It is striking that the decreased total SV number in *snt-1* mutants was suppressed in *snt-1*; *snt-3* double mutants (Fig. 4). This likely results from an accumulation of SVs due to the complete loss of evoked synaptic transmission in these double mutants.

Syts and vesicle size

This study revealed different roles for SNT-1 and SNT-3 in the regulation of vesicle size. The vesicle diameter and mEPSC amplitude were both increased in *snt-1* mutants (Fig. 1 and Fig. 4). This likely arises from a defect in endocytosis, leading to the release of abnormally large SVs, possibly including the irregular vesicles that accumulate in *snt-1* mutants, as previously reported (Jorgensen et al., 1995; Yu et al., 2013). A similar increase in vesicle diameter has been observed in other *C. elegans* mutants implicated in endocytosis (Gu et al., 2013; Mullen et al., 2012; Ritter et al., 2013; Zhang et al., 1998). Moreover, knockout of Syt1 in the fly NMJ also results in increased vesicle diameter (Lee et al., 2013), and prior studies have reported that, in addition to triggering exocytosis as a Ca^{2+} sensor, Syt1 also plays essential roles in endocytosis by interacting with endocytic proteins (Fergestad and Broadie, 2001; Lazzell et al., 2004; Phillips et al., 2000; Schivell et al., 2005). Furthermore, the role of Syt1 in endocytosis is Ca^{2+} dependent. Thus, SNT-1 and Syt1 have conserved functions in regulating vesicle size.

In contrast to *snt-1* mutants, the vesicle diameter was decreased by the loss of SNT-3, although we did not see a corresponding change in mEPSC amplitude in *snt-3* mutants, possibly because the decrease in vesicle size was relatively small. However, knockout of *snt-3* in the *snt-1* mutant background (i.e., *snt-1*; *snt-3* double mutant) produced a more profound decrease in vesicle diameter than that observed in the *snt-3* single mutants, suppressing the effects of SNT-1 on vesicle diameter, although abnormal numbers of irregular vesicles were still present (Fig. 4 E and Fig. S4). Moreover, overexpression of SNT-3 in *snt-1*; *snt-3* double mutants caused an even larger mEPSC amplitude than that obtained in *snt-1* mutants. These results reveal that SNT-1 and SNT-3 have opposing roles in regulating vesicle size. Based on these observations, it appears that both SNT-1 and SNT-3 are likely to be involved in the endocytic process, possibly functioning antagonistically, with SNT-1 promoting endocytosis and SNT-3 inhibiting it.

Functional importance of membrane tethering in fast and slow Ca^{2+} sensors

Syt was originally defined as a TM protein with cytoplasmic C2 domains, with all characterized Syt Ca^{2+} sensors possessing an N-terminal TM domain that tethers the proteins on distinct cellular membranes (Brose et al., 1992; Littleton et al., 1993; Perin et al., 1990; Sugita et al., 2001). One exception is the mouse Syt17 isoform, which does not possess an N-terminal TM domain (Kwon et al., 1996); however, recent studies have revealed that its C2 domains do not bind Ca^{2+} or trigger membrane fusion

(Ruhl et al., 2019). Our finding that SNT-3 lacks a TM domain but triggers Ca^{2+} -dependent slow neurotransmitter release in *C. elegans* indicates that membrane tethering may not be required for some Syt Ca^{2+} sensors. This notion is supported by in vitro-reconstituted membrane fusion assays demonstrating that cytoplasmic Syt1 is fully functional and can substitute for full-length Syt1 in mediating liposome fusion (Wang et al., 2011). However, in vivo experiments at the fly NMJ have shown that cytoplasmic Syt1 failed to restore fast synchronous neurotransmitter release (Lee and Littleton, 2015). Despite these paradoxical observations, we found that *C. elegans* SNT-1 that lacks the TM domain or the whole N terminus is still functional, as demonstrated by the ability to rescue locomotion and synaptic transmission (Fig. 9).

Notably, the evoked EPSCs rescued by cytoplasmic SNT-1 exhibited comparable synaptic delay to that rescued by full-length SNT-1 (Fig. 9), indicating that SNT-1 still functions as a fast Ca^{2+} sensor even when it is not tethered on SVs. Interestingly, the cytoplasmic region of vertebrate Syt1 retains the ability to synchronize SV release in response to a train stimulus (Díez-Arazola et al., 2020). In contrast, we show that SNT-3 is cytoplasmic but mediates delayed neurotransmitter release. Together, these results indicate that the release kinetics mediated by distinct Ca^{2+} sensors appears to be determined by their intrinsically different C2 domains rather than differences in their membrane association. However, disrupting SNT-1-SV tethering reduced the amplitude of fast neurotransmitter release without changing the quantal content of the RRP (Fig. 9). Thus, our results reveal an essential role of SNT-1-SV tethering in regulating the probability of neurotransmitter release. One possible explanation for this observation is that SV-tethered SNT-1 stabilizes primed SVs close to the sites of Ca^{2+} entry, thereby enhancing release probability. This notion is supported by the reduction in proximally docked SVs in *snt-1* mutants.

With the exception of mouse Syt17, SNT-3 is the only Syt homologue lacking a TM domain. We therefore considered the possibility that SNT-3 could be a homologue of other double-C2 domain-containing proteins, such as rabphilin-3A and Doc2, which both lack an N-terminal TM domain. However, several pieces of evidence do not support this notion. First, a phylogenetic analysis revealed that SNT-3 is closest to SNT-1 and the mouse Syt1/2, but not mouse rabphilin-3A or Doc2 (Fig. S11). Second, both rabphilin-3A and Doc2 have functional domains in their N termini, a Zn^{2+} finger domain in rabphilin-3A that binds to Rab-3, and a MID motif (Munc13 interaction domain) in Doc2 that binds to Munc13. In contrast, the SNT-3 N terminus, consisting of only 11 aa, does not appear to be functional. Third, the worm RBF-1, encoded by the *rbf-1* gene, appears to be the homologue of the mouse rabphilin-3A, displaying high sequence similarity (45% in the N-terminal Zn^{2+} domain and 48% in the C2 domain; Staunton et al., 2001). Our unpublished results show that synaptic transmission is not altered in either *rbf-1* mutants or the *snt-1;rbf-1* double mutants, suggesting that RBF-1 does not function as a Ca^{2+} sensor at *C. elegans* NMJs. Moreover, rabphilin-3A and RBF-1 are known to be localized on SVs (Staunton et al., 2001), whereas SNT-3, based on our results, is not on SVs (Fig. 2). Fourth, Doc2 has been shown to be

required for baseline transmission, including asynchronous release in cultured hippocampal neurons (Yao et al., 2011) and spontaneous release in cultured cortical neurons (Courtney et al., 2018; Pang et al., 2011). In contrast, the *snt-3* single-mutant worms do not exhibit any synaptic transmission defect, suggesting that SNT-3 is functionally different from Doc2. Finally, our findings that cytoplasmic SNT-1 can still trigger spontaneous and fast evoked neurotransmitter release indicate that a TM domain is not required for a Syt to act as a Ca^{2+} sensor. Together, these observations support the classification of SNT-3 as a member of the Syt protein family.

Additional functions of SNT-3?

Our data further suggest that SNT-3 has additional functions beyond serving as a Ca^{2+} sensor in the nervous system. The synaptic terminal areas were decreased in *snt-3* mutants (Fig. 4), indicating that SNT-3 is required to maintain a normal bouton size, although the mechanism of this regulation is unknown. One possibility is that the smaller SV diameter observed in *snt-3* mutants, combined with potentially higher levels of endocytosis, results in less membrane incorporation and smaller terminal size.

In addition to functioning at presynaptic sites, SNT-3 may also have a postsynaptic role, as indicated by its expression in body wall muscles. Recent studies have revealed that several Syts, such as Syt1, Syt7, and Syt3, play essential roles in postsynaptic AMPA receptor internalization, thereby regulating synaptic strength and long-term potentiation (Awasthi et al., 2019; Wu et al., 2017). Blocking postsynaptic expression of these Syts does not impair basal synaptic transmission or the levels of AMPA receptors. In agreement with these results, our data showed that ACh-activated currents were normal in *snt-3* mutants (Fig. S5), suggesting that the function and surface levels of AChRs are unaltered. It is still possible that SNT-3 is required for activity-induced receptor trafficking and endocytosis. These observations, together with changes in vesicle size, provide intriguing future research directions of SNT-3.

Materials and methods

Strains

Animals were cultivated at RT on nematode growth medium agar plates seeded with OP50 bacteria. On the day before experiments, L4 larval stage animals were transferred to fresh plates seeded with OP50 bacteria for all the electrophysiological recordings. The following strains were used: WT, N2 bristol; NM204 *snt-1(md290)*; TM5776 *snt-3(tm5776)*; CX1034 *snt-3(ky1034)*; ZTH666 *snt-1(md290)*; *snt-3(tm5776)*; ZTH795 *snt-1(md290)*; *snt-3(ky1034)*; ZX460 *zxIs6 [Punc-17::ChR2(H134R)::YFP]*; ZTH62 *zxIs6*; *snt-1(md290)*; ZTH960 *zxIs6*; *snt-3(tm5776)*; EG5793 *oxSi91 [Punc-17::ChIEF::mCherry]*; ZTH655 *oxSi91*; *snt-3(tm5776)*; ZTH728 *hztEx375 [Psnt-3::mApple]*; ZTH760 *hztEx375*; *vsIs48 [Punc-17::GFP]*; ZTH765 *hztEx375*; *juIs76 [Punc-25::GFP]*; ZTH380 *hztEx380 [Punc-129::SNT-1::mApple]*; ZTH674 *hztEx381 [Punc-129::SNT-3::mApple]*; *hztEx366 [Punc-129::SNT-1::GFP]*; ZTH675 *hztEx381*; *nuIs431 [Punc-129::RAB-3::GFP]*; ZTH673 *hztEx381*; *nuIs165 [Punc-129::UNC-10::GFP]*;

ZTH664 hztEx381; nuIs184 [Punc-129::APT-4::GFP]; ZTH394 nuIs165; hztEx380 [Punc-129::SNT-1::mApple]; ZTH739 nuIs165; hztEx390 [Punc-129::SNT-1^{ΔN}::mApple]; ZTH867 nuIs165; hztEx391 [Punc-129::SNT-1^{ΔTM}::mApple]; ZTH846 nuIs165; hztEx392 [Punc-129::SNT-1(C2A)::mApple]; ZTH833 nuIs165; hztEx393 [Punc-129::SNT-1(C2B)::mApple]; ZTH746 hztEx380; unc-13(s69); ZTH748 hztEx381; unc-13(s69); ZTH 679 hztEx381; snt-1(md290); JSD1039 tauSi4 [Psnb-1::UNC-13L]; unc-13(s69); ZTH793 tauSi4; unc-13(s69); snt-3(tm5776); ZTH456 hztSi1 [Psnb-1::UNC-13MR]; unc-13(s69); ZTH759 hztSi1; unc-13(s69); snt-3(tm5776); ZTH403 hztEx001 [Psnb-1::SNT-1]; snt-1(md290); ZTH730 hztEx387 [Psnb-1::SNT-1^{ΔN}]; snt-1(md290); ZTH734 hztEx388 [Psnb-1::SNT-1^{ΔTM}]; snt-1(md290); ZTH672 hztEx149 [Prab-3::SNT-3]; snt-3(tm5776); ZTH698 hztEx149; snt-1(md290); snt-3(tm5776); ZTH719 hztSi8 [Prab-3::SNT-3]; snt-3(tm5776); ZTH688 hztEx001 [Psnb-1::SNT-1]; snt-1(md290); snt-3(tm5776); ZTH412 hztEx412 [Psnb-1::SNT-1^{C2A D3,4N}]; snt-1(md290); ZTH413 hztEx413 [Psnb-1::SNT-1^{C2B D3,4N}]; snt-1(md290); ZTH254 hztEx254 [Psnb-1::SNT-1^{C2AB D3,4N}]; snt-1(md290); ZTH723 hztEx412; snt-1(md290); snt-3(tm5776); ZTH687 hztEx413; snt-1(md290); snt-3(tm5776); ZTH713 hztEx254; snt-1(md290); snt-3(tm5776); ZTH758 hztEx254; hztEx149 [Prab-3::SNT-3]; snt-1(md290); snt-3(tm5776); ZTH775 hztEx152 [Prab-3::SNT-3^{C2A D3,4N}]; snt-1(md290); snt-3(tm5776); ZTH841 hztEx153 [Prab-3::SNT-3^{C2B D3,4N}]; snt-1(md290); snt-3(tm5776); and ZTH865 hztEx254; hztEx151; snt-1(md290); snt-3(tm5776).

Constructs

A 1.3-kb cDNA corresponding to *snt-1a* was amplified by PCR from the N2 cDNA library and inserted into MCSII (multiple cloning site II) of the JB6 vector between the KpnI and NotI sites. The *snb-1* promoter was inserted into MCSI between the SphI and BamHI sites. The plasmids used for expression of GFP or mApple were based on the JB6 backbone under the control of the *unc-129* promoter. The cDNA of *snt-3* was cloned into a miniMOS vector backbone phzt609 (a derivative of pCFJ910) between XmaI and NotI after the *rab-3* promoter.

Primers used in this study

snt-3(ky1034) genotyping—forward: 5'-TTCAGTGAGCTTATG TTGGTGT-3', reverse: 5'-ATTTTCGAATTCAAAGCAAAGGCA-3'; snt-3(tm5776) genotyping—forward: 5'-GGTTCGACAACTGTG GCCA-3', reverse: 5'-GCCGAAGAGTTACCTGCCAT-3'; Prab-3::SNT-3—forward: 5'-AGCCCGGAAAAAATGTCAGTGTCCAAA AAGAA-3', reverse: 5'-TCGCGGCCGCTAATCATCATTGAAAG G-3'; Psnt-3::mApple—forward: 5'-TTGGCTAGCTCAGTGAT ACAATGCCCC-3', reverse: 5'-TCAGATCTACTGCAAAGAAAA TCATTAGTACACCA-3'; Punc-129::SNT-1::mApple—forward: 5'-ACATGGTACCATGGTGAATTAGACTTTTCGTGCG-3', reverse: 5'-CGGCGGCCGCTTATTTCTTATCATCTTTCTTATCACCTTCTT CT-3'; Punc-129::SNT-3::mApple—forward: 5'-AGCCCGGAAA AAAATGTCAGTGTCCAAAAGAA-3', reverse: 5'-TCGCGGCCG CCTAATCATCATTGAAAGG-3'; SNT-1(C2A D3,4N) mutations— forward: 5'-GTCTTTGCAATTTATAATTTCAATCGGTTAGTAAG CAC-3', reverse: 5'-GTGCTTACTGAACCGATTGAAATTATAAAT TGCAAAGAC-3'; SNT-1(C2B D3,4N) mutations forward: 5'-GAT CACTGTGATGAATTATAATAAACTTGGATCCAAT-3'; SNT-1(C2B D3,4N) mutations reverse: 5'-ATTGGATCCAAGTTTATTATAATT

CATCACAGTGATC-3'; SNT-3(C2A D3,4N) mutations—forward: 5'-GTGTTCAATTTTAAATCGATTTGGAAAAACATGACCAGA-3', reverse: 5'-CGATTAATAATTGAACACATTAAGAACCAGTTTGA CC-3'; SNT-3(C2B D3,4N) mutations—forward: 5'-TCCAATTAC AATAGAGTTGGTTCCAATGAACG-3', reverse: 5'-ACTCTATTG TAATTGGATACCGTCACATGAAGGT-3'; Prab-3::NSNT-1-SNT-3—forward: 5'-TCCCCGGGATGGTGAAATTAGACTTTTC-3', Prab-3::NSNT-1-SNT-3 inner—reverse: 5'-GGACTGATTTTTCTTC AGCTTGTCTTTTTTCATTTT-3'; Prab-3::NSNT-1-SNT-3 inner— forward: 5'-GAAAAATCAGTGTCCAAAAAGAAAGACG-3', Prab-3:: NSNT-1-SNT-3—reverse: 5'-TCGCGGCCGCTAATCATCATTGAA AGG-3'; Psnb-1::SNT-1(ΔN)—forward: 5'-CCATGGAAGAAGTGAAC TTGGAAGGA-3', reverse: 5'-CACTTCTTCCATGTTACCGGTGGAATT CG-3'; Psnb-1::SNT-1(ΔTM)—forward: 5'-TGCAACAACGGAAGT TATTTGGAAAAAAGCGGC-3', reverse: 5'-CITTCGGTTGTTGCAT AACTTTTCTTCCACAACGTCT-3'; Punc-129::C2A::mApple—forward: 5'-TCCCCGGGAAAAAATGGAAGAAGTGAACCTG-3', reverse: 5'-TAGCGGCCGCGGAATGAGAAGTGTGTC-3'; Punc-129::C2B::mApple— forward: 5'-TCCCCGGGAAAAAATGGATGACAAAAGAAGCTGAG-3', reverse: 5'-TAGCGGCCGCTCCCAATAGACACCTTC-3'; pET28a snt-1 C2AB—forward: 5'-ATTCGAGTCAAAGAAGAAGTGAAC-3', reverse: 5'-GGTGCTCGAGTTATTTCTTATCATCTTT-3'; pET28a SNT-3—forward: 5'-ATTCGAGTCAATGTCAGTGTCCAAAAAG-3', reverse: 5'-GGTGCTCGAGTCAATCATCATTGAAAGG-3'.

Transgenes and germline transformation

Transgenic strains were isolated by microinjection of various plasmids by using either Pmyo-2::NLS-GFP (KP#1106) or Pmyo-2::NLS-mCherry (KP#1480) as the coinjection marker. The single-copy insertion lines were generated by using miniMos transposon (Frøkjær-Jensen et al., 2014).

Locomotion and behavioral assays

Young adult animals were washed with a drop of PBS and then transferred to fresh nematode growth medium plates with no bacterial lawn (30 worms per plate). Worm movement recordings (under room temperature 22°C) were started 10 min after the worms were transferred. A 2-min digital video of each plate was captured at a 3.75-Hz frame rate by WormLab System (MBF Bioscience). Average speed and tracks were generated for each animal by using WormLab software.

Fluorescence imaging

Animals were immobilized on 2% agarose pads with 20 mM levamisole. Fluorescence imaging was performed on a spinning-disk confocal system (3i Yokogawa W1 SDC, Evolve EMCCD; Photometrics) controlled by Slidebook 6.0 software. Animals were imaged with an Olympus 100× 1.4 NA Plan-Apochromat objective at RT. A Z series of optical sections was acquired in 0.13-μm steps. Images were deconvolved with Huygens Professional version 16.10 (Scientific Volume Imaging) and processed to yield maximum-intensity projections by using ImageJ version 1.53a (Wayne Rasband, National Institutes of Health).

Recombinant protein production and purification

cDNA encoding the C2AB fragment of *C. elegans* SNT-1 (WT and the SNT-1 D3,4N) and SNT-3 (WT and the SNT-3 D3,4N mutant)

was subcloned into the pET28a vector. Recombinant proteins were expressed as N-terminal his6-tagged fusion proteins in the *Escherichia coli* strain BL21(DE3). Bacteria overnights (3 ml) were transferred to 500 ml of Terrific Broth media. The culture was further grown at 37°C to reach OD₆₀₀ of 0.8. IPTG was added to induce protein production (final [IPTG] = 0.2 mM), and the culture was further grown overnight (shaking at 200 rpm at 15°C). Bacteria was harvested by using centrifugation and was lysed by sonication in the Hepes buffer containing 20 mM Hepes (pH 8.0), 300 mM NaCl, and 15 mM imidazole. Proteins were incubated overnight with Ni-NTA agarose beads. Bound proteins were washed three times with Hepes buffer and eluted by using the elution buffer (20 mM Hepes, pH 8.0, 300 mM NaCl, and 200 mM imidazole). Purified proteins were dialyzed against the dialysis buffer (50 mM Hepes, pH 7.4, 150 mM NaCl, and 1 mM DTT).

Liposomes

Phospholipids were dried under compressed nitrogen for 30 min. Residue chloroform was removed by using a Freeze Dry System (FreeZone 2.5 L Benchtop Freeze Dry) for 2 h. Dried lipids were reconstituted by vortexing in the Hepes buffer (50 mM Hepes, pH 7.4, and 150 mM NaCl). Liposomes were prepared by using mini-extruders (Avanti Polar Lipids), 200 nm Nuclepore Track-Etch membranes (Cat. #7007865; Whatman), and filter supports (Cat. #610014; Avanti Polar Lipids), as previously described.

Liposome cosedimentation

Recombinant proteins were prespined in open-top thickwall polycarbonate tubes (Cat. #349622; Beckman Coulter Optima) by using a Beckman TLA100.3 rotor at 65,000 rpm for 3 h to remove aggregates. Next, prespined protein (2 μM) was incubated with liposomes (1 mM total lipids; 75% zwitterionic dioleoylphosphatidylcholine/25% anionic dioleoylphosphatidylserine) in Hepes buffer with either 1 mM EGTA or 1 mM Ca²⁺ at RT for 30 min. Protein liposome samples were centrifuged in open-top thickwall polycarbonate tubes (Cat. #343775; Beckman Coulter Optima) by using a Beckman TLA100 rotor at 65,000 rpm for 1.5 h. The supernatant and pellet were collected and analyzed by using electrophoresis. Approximately 18% of total, supernatant, and pellet samples were loaded onto SDS-PAGE gels. Protein bands were visualized with Coomassie blue staining and were analyzed by using ImageJ.

ITC

ITC experiments were performed by using a Microcal ITC200 instrument (Malvern) at 298 K. Prior to ITC experiments, SNT-3 was incubated with 10 mM EDTA for 2 h to remove any metal ions bound to the protein and dialyzed excessively against the working buffer (50 mM Hepes, pH 7.5, 200 mM NaCl, 2 mM β-mercaptoethanol) to remove EDTA. 50 μM SNT-3 was then titrated against 2 mM Ca²⁺ ions by using a series of 13 injections of 3.22 μl each with 180-s intervals. The dissociation constant (1/*K_a*), enthalpy of binding (Δ*H*), and stoichiometry of the binding reaction (*N*) were calculated by fitting the data to a single-site binding model by using MicroCal PEAQ-ITC software. The Gibbs

free energy of binding (Δ*G*) and entropy of the reaction (Δ*S*) were calculated by using the equations Δ*G* = RTln(*K_a*) and Δ*G* = Δ*H* – TΔ*S*, respectively. Experiments were performed in triplicate to check for reproducibility, with the average values of three experiments reported. The SDs of each parameter were also calculated from the three trials.

Electrophysiology

Electrophysiology was conducted on dissected *C. elegans*, as previously described (Hu et al., 2012). Worms were superfused in an extracellular solution containing 127 mM NaCl, 5 mM KCl, 26 mM NaHCO₃, 1.25 mM NaH₂PO₄, 20 mM glucose, 1 mM CaCl₂, and 4 mM MgCl₂; and bubbled with 5% CO₂, 95% O₂ at 20°C. Whole-cell recordings were performed at –60 mV for all EPSCs, including mEPSCs, evoked EPSCs, and sucrose-evoked responses. The internal solution contained 105 mM CH₃O₃SCs, 10 mM CsCl, 15 mM CsF, 4 mM MgCl₂, 5 mM EGTA, 0.25 mM CaCl₂, 10 mM Hepes, and 4 mM Na₂ATP, adjusted to pH 7.2 by using CsOH. Stimulus-evoked EPSCs were obtained by placing a borosilicate pipette (5–10 μm) near the ventral nerve cord (one muscle distance from the recording pipette) and applying a 0.4-ms, 85-μA square pulse. Sucrose-evoked release was triggered by a 5-s application of 0.5 M sucrose dissolved in normal bath solution. The pipette containing hypertonic sucrose was placed at the end of the patched muscle cell. A single wavelength LED (470 nm; Thorlabs) was used to provide optogenetic stimulation. The intensity was adjusted to the maximal level. All recordings were performed at RT (22°C).

EM

Samples were prepared by using high-pressure freeze fixation (Weimer et al., 2006). ~30 young adult hermaphrodites were placed in each specimen chamber containing *E. coli* and were frozen at –180°C under high pressure (Leica SPF HPM 100). Frozen specimens then underwent freeze substitution (Leica Reichert AFS) during which the samples were held at –90°C for 107 h in 0.1% tannic acid and 2% OsO₄ in anhydrous acetone. The temperature was then increased at 5°C/h to –20°C, kept at –20°C for 14 h, and increased by 10°C/h to 20°C. After fixation, samples were infiltrated with 50% Epon/acetone for 4 h, 90% Epon/acetone for 18 h, and 100% Epon for 5 h. Finally, samples were embedded in Epon and incubated for 48 h at 65°C. Ultrathin (40 nm) serial sections were cut by using a Leica Ultracut 6 and collected on formvar-covered, carbon-coated copper grids (FCF2010-Cu; EMS). Poststaining was performed by using 2.5% aqueous uranyl acetate for 4 min, followed by Reynolds lead citrate for 2 min. Images were acquired by using a JEOL JEM-1220 transmission EM operating at 80 kV with a Gatan digital camera at a magnification of 100k. Images were collected from the ventral nerve cord region anterior to the vulva for all genotypes. Cholinergic synapses were identified on the basis of their typical morphology (White et al., 1986). A synapse was defined as a series of sections (profiles) containing a dense projection and two flanking sections on both sides without dense projections. A docked SV was defined as an SV whose membrane was morphologically contacting the plasma membrane (distance to plasma membrane = 0 nm). Image acquisition and analysis with

National Institutes of Health ImageJ/Fiji software were performed blinded for genotype.

Data acquisition and statistical analysis

All electrophysiological data were obtained by using a HEKA EPC10 double amplifier (HEKA Elektronik) filtered at 2 kHz and analyzed with open-source scripts developed by Eugene Mosharov in Igor Pro 7 (Wavemetrics). All imaging data were analyzed in ImageJ software. Each set of data represents the mean \pm SEM of an indicated number of animals. To analyze mEPSCs and mIPSCs, a 4-pA peak threshold was preset, above which release events are clearly distinguished from background noise. The analyzed results were rechecked by eye to ensure that the release events were accurately selected.

Statistical analysis

All data were statistically analyzed in Prism 8 software. Normality distribution of the data was determined by the D'Agostino-Pearson normality test. When the data followed a normal distribution, an unpaired Student's *t* test (two tailed) or one-way ANOVA was used to evaluate the statistical significance. In other cases, a Mann-Whitney test or one-way ANOVA following Kruskal-Wallis test was used. A summary of all electrophysiological data is provided in Table S1, with the results presented as mean \pm SEM.

Data availability

Data generated or analyzed during this study are included in this published article or available upon request.

Online supplemental material

Fig. S1 shows the domain structure of all Syt isoforms in *C. elegans*. Fig. S2 shows the quantification of body length in WT, *snt-1*, *snt-3*, and *snt-1;snt-3* mutants. Fig. S3 shows the averaged decay of mEPSCs in WT, *snt-1*, *snt-3*, *snt-1;snt-3*, and SNT-3 neuronal rescue animals. Fig. S4 shows the cumulative probability of mEPSCs in WT, *snt-1*, *snt-1;snt-3*, and SNT-3 neuronal rescue animals. Fig. S5 shows the quantification of ACh-activated current in WT and *snt-3* mutants. Fig. S6 shows the docked SV distribution and the mEPSC event distribution in WT, *snt-1*, *snt-3*, and *snt-1;snt-3* mutants. Fig. S7 shows the cumulative probability of mEPSCs in *snt-1;snt-3*, SNT-3 neuronal rescue, SNT-3^{C2A D3,4N} neuronal rescue, and SNT-3^{C2B D3,4N} neuronal rescue animals. Fig. S8 shows the colocalization of UNC-10 with the C2A or C2B domain of SNT-1. Fig. S9 shows the quantification of body length in WT, *snt-1* mutants, SNT-1^{ΔTM}, and SNT-1^{ΔN} rescue animals. Fig. S10 shows the averaged decay of mEPSCs in WT, *snt-1* mutants, SNT-1^{FL}, SNT-1^{ΔTM}, and SNT-1^{ΔN} rescue animals. Fig. S11 shows the phylogenetic analysis of Syt isoforms in *C. elegans*. Table S1 summarizes the electrophysiological data in this study.

Acknowledgments

We thank the *C. elegans* Genetics Stock Center for strains and reagents. We thank Rowan Tweedale for critically reading the manuscript. This work made use of the BioCryo facility of

Northwestern University's NUANCE Center, which has received support from the Soft and Hybrid Nanotechnology Experimental (SHyNE) Resource (NSF ECCS-1542205), the MRSEC program (NSF DMR-1720139) at the Materials Research Center, the International Institute for Nanotechnology (IIN), and the State of Illinois, through the IIN. It also made use of the CryoCluster equipment, which has received support from the magnetic resonance imaging program (NSF DMR-1229693). Images were acquired using instruments in the Electron Microscopy Core of the University of Illinois at Chicago's Research Resources Center.

This work was supported by an Australian Research Council Discovery Project grant (DP160100849; Z. Hu), a National Health and Medical Research Council project grant (GNT1122351; Z. Hu), a NARSAD Young Investigator grant from the Brain and Behavior Research Foundation (24980; Z. Hu), a National Institutes of Health, National Eye Institute research grant (1R21EY029450-01; J. Liu, Z. Hu, and Pablo Blinder), a National Health and Medical Research Council project grant (GNT1138083; B. Collins) a National Health and Medical Research Council senior research fellowship (APP1136021; B. Collins), and a National Institutes of Health grant (R01GM127857; J. Bai).

The authors declare no competing financial interests.

Author contributions: L. Li: conceptualization, investigation, and writing—review and editing; H. Liu: conceptualization, investigation, and writing—review and editing; M. Krout: investigation, and writing—review and editing; J. Richmond: supervision, funding acquisition, investigation, and writing—review and editing; Y. Wang: investigation; J. Bai: supervision, funding acquisition, investigation, and writing—review and editing; S. Weeratunga: investigation; B.M. Collins: supervision, funding acquisition, and investigation; D. Ventimiglia: investigation; Y. Yu: investigation; J. Xia: investigation; J. Tang: investigation; J. Liu: investigation; and Z. Hu: supervision, funding acquisition, investigation, and writing—original draft, review, and editing.

Submitted: 23 August 2020

Revised: 19 December 2020

Accepted: 15 January 2021

References

- Awasthi, A., B. Ramachandran, S. Ahmed, E. Benito, Y. Shinoda, N. Nitzan, A. Heukamp, S. Rannio, H. Martens, J. Barth, et al. 2019. Synaptotagmin-3 drives AMPA receptor endocytosis, depression of synapse strength, and forgetting. *Science*. 363:eav1483. <https://doi.org/10.1126/science.aav1483>
- Bacaj, T., D. Wu, X. Yang, W. Morishita, P. Zhou, W. Xu, R.C. Malenka, and T.C. Südhof. 2013. Synaptotagmin-1 and synaptotagmin-7 trigger synchronous and asynchronous phases of neurotransmitter release. *Neuron*. 80:947–959. <https://doi.org/10.1016/j.neuron.2013.10.026>
- Bacaj, T., D. Wu, J. Burré, R.C. Malenka, X. Liu, and T.C. Südhof. 2015. Synaptotagmin-1 and -7 Are Redundantly Essential for Maintaining the Capacity of the Readily-Releasable Pool of Synaptic Vesicles. *PLoS Biol*. 13:e1002267. <https://doi.org/10.1371/journal.pbio.1002267>
- Becherer, U., and J. Rettig. 2006. Vesicle pools, docking, priming, and release. *Cell Tissue Res*. 326:393–407. <https://doi.org/10.1007/s00441-006-0243-z>
- Bouhours, B., E. Gjoni, O. Kochubey, and R. Schneggenburger. 2017. Synaptotagmin2 (Syt2) Drives Fast Release Redundantly with Syt1 at the

- Output Synapses of Parvalbumin-Expressing Inhibitory Neurons. *J. Neurosci.* 37:4604–4617. <https://doi.org/10.1523/JNEUROSCI.3736-16.2017>
- Brose, N., A.G. Petrenko, T.C. Südhof, and R. Jahn. 1992. Synaptotagmin: a calcium sensor on the synaptic vesicle surface. *Science*. 256:1021–1025. <https://doi.org/10.1126/science.1589771>
- Chang, S., T. Trimbuch, and C. Rosenmund. 2018. Synaptotagmin-1 drives synchronous Ca²⁺-triggered fusion by C₂B-domain-mediated synaptic-vesicle-membrane attachment. *Nat. Neurosci.* 21:33–40. <https://doi.org/10.1038/s41593-017-0037-5>
- Chapman, E.R. 2008. How does synaptotagmin trigger neurotransmitter release? *Annu. Rev. Biochem.* 77:615–641. <https://doi.org/10.1146/annurev.biochem.77.062005.101135>
- Chapman, E.R., and R. Jahn. 1994. Calcium-dependent interaction of the cytoplasmic region of synaptotagmin with membranes. Autonomous function of a single C2-homologous domain. *J. Biol. Chem.* 269:5735–5741. [https://doi.org/10.1016/S0021-9258\(17\)37523-3](https://doi.org/10.1016/S0021-9258(17)37523-3)
- Chapman, E.R., P.I. Hanson, S. An, and R. Jahn. 1995. Ca²⁺ regulates the interaction between synaptotagmin and syntaxin 1. *J. Biol. Chem.* 270:23667–23671. <https://doi.org/10.1074/jbc.270.40.23667>
- Chen, C., I. Arai, R. Satterfield, S.M. Young Jr., and P. Jonas. 2017a. Synaptotagmin 2 Is the Fast Ca²⁺ Sensor at a Central Inhibitory Synapse. *Cell Rep.* 18:723–736. <https://doi.org/10.1016/j.celrep.2016.12.067>
- Chen, C., R. Satterfield, S.M. Young Jr., and P. Jonas. 2017b. Triple Function of Synaptotagmin 7 Ensures Efficiency of High-Frequency Transmission at Central GABAergic Synapses. *Cell Rep.* 21:2082–2089. <https://doi.org/10.1016/j.celrep.2017.10.122>
- Courtney, N.A., J.S. Briguglio, M.M. Bradberry, C. Greer, and E.R. Chapman. 2018. Excitatory and Inhibitory Neurons Utilize Different Ca²⁺ Sensors and Sources to Regulate Spontaneous Release. *Neuron*. 98:977–991.e5. <https://doi.org/10.1016/j.neuron.2018.04.022>
- Courtney, N.A., H. Bao, J.S. Briguglio, and E.R. Chapman. 2019. Synaptotagmin 1 clamps synaptic vesicle fusion in mammalian neurons independent of complexin. *Nat. Commun.* 10:4076. <https://doi.org/10.1038/s41467-019-12015-w>
- Díez-Arazola, R., M. Meijer, Q. Bourgeois-Jaarsma, L.N. Cornelisse, M. Verhage, and A.J. Groffen. 2020. Doc2 Proteins Are Not Required for the Increased Spontaneous Release Rate in Synaptotagmin-1-Deficient Neurons. *J. Neurosci.* 40:2606–2617. <https://doi.org/10.1523/JNEUROSCI.0309-19.2020>
- Fergestad, T., and K. Brodie. 2001. Interaction of stoned and synaptotagmin in synaptic vesicle endocytosis. *J. Neurosci.* 21:1218–1227. <https://doi.org/10.1523/JNEUROSCI.21-04-01218.2001>
- Frøkjær-Jensen, C., M.W. Davis, M. Sarov, J. Taylor, S. Flibotte, M. LaBella, A. Pozniakovskiy, D.G. Moerman, and E.M. Jorgensen. 2014. Random and targeted transgene insertion in *Caenorhabditis elegans* using a modified Mos1 transposon. *Nat. Methods.* 11:529–534. <https://doi.org/10.1038/nmeth.2889>
- Geppert, M., Y. Goda, R.E. Hammer, C. Li, T.W. Rosahl, C.F. Stevens, and T.C. Südhof. 1994. Synaptotagmin I: a major Ca²⁺ sensor for transmitter release at a central synapse. *Cell*. 79:717–727. [https://doi.org/10.1016/0092-8674\(94\)90556-8](https://doi.org/10.1016/0092-8674(94)90556-8)
- Gerber, S.H., J.C. Rah, S.W. Min, X. Liu, H. de Wit, I. Dulubova, A.C. Meyer, J. Rizo, M. Arancillo, R.E. Hammer, et al. 2008. Conformational switch of syntaxin-1 controls synaptic vesicle fusion. *Science*. 321:1507–1510. <https://doi.org/10.1126/science.1163174>
- Gracheva, E.O., G. Hadwiger, M.L. Nonet, and J.E. Richmond. 2008. Direct interactions between *C. elegans* RAB-3 and Rim provide a mechanism to target vesicles to the presynaptic density. *Neurosci. Lett.* 444:137–142. <https://doi.org/10.1016/j.neulet.2008.08.026>
- Gu, M., Q. Liu, S. Watanabe, L. Sun, G. Hollopeter, B.D. Grant, and E.M. Jorgensen. 2013. AP2 hemicomplexes contribute independently to synaptic vesicle endocytosis. *eLife*. 2:e00190. <https://doi.org/10.7554/eLife.00190>
- Guan, Z., M.C. Quiñones-Frías, Y. Akbergenova, and J.T. Littleton. 2020. *Drosophila* Synaptotagmin 7 negatively regulates synaptic vesicle release and replenishment in a dosage-dependent manner. *eLife*. 9:e55443. <https://doi.org/10.7554/eLife.55443>
- Hall, D.H., and E.M. Hedgecock. 1991. Kinesin-related gene unc-104 is required for axonal transport of synaptic vesicles in *C. elegans*. *Cell*. 65:837–847. [https://doi.org/10.1016/0092-8674\(91\)90391-B](https://doi.org/10.1016/0092-8674(91)90391-B)
- Hammarlund, M., M.T. Palfreyman, S. Watanabe, S. Olsen, and E.M. Jorgensen. 2007. Open syntaxin docks synaptic vesicles. *PLoS Biol.* 5:e198. <https://doi.org/10.1371/journal.pbio.0050198>
- Hu, Z., S. Hom, T. Kudze, X.J. Tong, S. Choi, G. Aramuni, W. Zhang, and J.M. Kaplan. 2012. Neurexin and neuroligin mediate retrograde synaptic inhibition in *C. elegans*. *Science*. 337:980–984. <https://doi.org/10.1126/science.1224896>
- Hu, Z., X.J. Tong, and J.M. Kaplan. 2013. UNC-13L, UNC-13S, and Tomosyn form a protein code for fast and slow neurotransmitter release in *Caenorhabditis elegans*. *eLife*. 2:e00967. <https://doi.org/10.7554/eLife.00967>
- Hua, S.Y., A. Syed, T.C. Aupérin, and L. Tong. 2014. The cytoplasmic domain of rat synaptotagmin I enhances synaptic transmission. *Cell. Mol. Neurobiol.* 34:659–667. <https://doi.org/10.1007/s10571-014-0040-2>
- Hui, E., C.P. Johnson, J. Yao, F.M. Dunning, and E.R. Chapman. 2009. Synaptotagmin-mediated bending of the target membrane is a critical step in Ca(2+)-regulated fusion. *Cell*. 138:709–721. <https://doi.org/10.1016/j.cell.2009.05.049>
- Imig, C., S.W. Min, S. Krinner, M. Arancillo, C. Rosenmund, T.C. Südhof, J. Rhee, N. Brose, and B.H. Cooper. 2014. The morphological and molecular nature of synaptic vesicle priming at presynaptic active zones. *Neuron*. 84:416–431. <https://doi.org/10.1016/j.neuron.2014.10.009>
- Jackman, S.L., J. Turecek, J.E. Belinsky, and W.G. Regehr. 2016. The calcium sensor synaptotagmin 7 is required for synaptic facilitation. *Nature*. 529:88–91. <https://doi.org/10.1038/nature16507>
- Jorgensen, E.M., E. Hartwig, K. Schuske, M.L. Nonet, Y. Jin, and H.R. Horvitz. 1995. Defective recycling of synaptic vesicles in synaptotagmin mutants of *Caenorhabditis elegans*. *Nature*. 378:196–199. <https://doi.org/10.1038/378196a0>
- Kochubey, O., and R. Schneggenburger. 2011. Synaptotagmin increases the dynamic range of synapses by driving Ca²⁺-evoked release and by clamping a near-linear remaining Ca²⁺ sensor. *Neuron*. 69:736–748. <https://doi.org/10.1016/j.neuron.2011.01.013>
- Kochubey, O., N. Babai, and R. Schneggenburger. 2016. A Synaptotagmin Isoform Switch during the Development of an Identified CNS Synapse. *Neuron*. 91:1183. <https://doi.org/10.1016/j.neuron.2016.08.024>
- Kwon, O.J., H. Gainer, S. Wray, and H. Chin. 1996. Identification of a novel protein containing two C2 domains selectively expressed in the rat brain and kidney. *FEBS Lett.* 378:135–139. [https://doi.org/10.1016/0014-5793\(95\)01430-6](https://doi.org/10.1016/0014-5793(95)01430-6)
- Lazzell, D.R., R. Belizaire, P. Thakur, D.M. Sherry, and R. Janz. 2004. SV2B regulates synaptotagmin 1 by direct interaction. *J. Biol. Chem.* 279:52124–52131. <https://doi.org/10.1074/jbc.M407502200>
- Lee, J., and J.T. Littleton. 2015. Transmembrane tethering of synaptotagmin to synaptic vesicles controls multiple modes of neurotransmitter release. *Proc. Natl. Acad. Sci. USA*. 112:3793–3798. <https://doi.org/10.1073/pnas.1420312112>
- Lee, J., Z. Guan, Y. Akbergenova, and J.T. Littleton. 2013. Genetic analysis of synaptotagmin C2 domain specificity in regulating spontaneous and evoked neurotransmitter release. *J. Neurosci.* 33:187–200. <https://doi.org/10.1523/JNEUROSCI.3214-12.2013>
- Li, L., H. Liu, W. Wang, M. Chandra, B.M. Collins, and Z. Hu. 2018. SNT-1 Functions as the Ca²⁺ Sensor for Tonic and Evoked Neurotransmitter Release in *Caenorhabditis Elegans*. *J. Neurosci.* 38:5313–5324. <https://doi.org/10.1523/JNEUROSCI.3097-17.2018>
- Li, L., H. Liu, Q. Hall, W. Wang, Y. Yu, J.M. Kaplan, and Z. Hu. 2019. A Hyperactive Form of unc-13 Enhances Ca²⁺ Sensitivity and Synaptic Vesicle Release Probability in *C. elegans*. *Cell Rep.* 28:2979–2995.e4. <https://doi.org/10.1016/j.celrep.2019.08.018>
- Littleton, J.T., M. Stern, K. Schulze, M. Perin, and H.J. Bellen. 1993. Mutational analysis of *Drosophila* synaptotagmin demonstrates its essential role in Ca(2+)-activated neurotransmitter release. *Cell*. 74:1125–1134. [https://doi.org/10.1016/0092-8674\(93\)90733-7](https://doi.org/10.1016/0092-8674(93)90733-7)
- Liu, H., C. Dean, C.P. Arthur, M. Dong, and E.R. Chapman. 2009a. Autapses and networks of hippocampal neurons exhibit distinct synaptic transmission phenotypes in the absence of synaptotagmin I. *J. Neurosci.* 29:7395–7403. <https://doi.org/10.1523/JNEUROSCI.1341-09.2009>
- Liu, Q., G. Hollopeter, and E.M. Jorgensen. 2009b. Graded synaptic transmission at the *Caenorhabditis elegans* neuromuscular junction. *Proc. Natl. Acad. Sci. USA*. 106:10823–10828. <https://doi.org/10.1073/pnas.0903570106>
- Liu, H., L. Li, W. Wang, J. Gong, X. Yang, and Z. Hu. 2018. Spontaneous Vesicle Fusion Is Differentially Regulated at Cholinergic and GABAergic Synapses. *Cell Rep.* 22:2334–2345. <https://doi.org/10.1016/j.celrep.2018.02.023>
- Liu, H., L. Li, D. Nedelcu, Q. Hall, L. Zhou, W. Wang, Y. Yu, J.M. Kaplan, and Z. Hu. 2019. Heterodimerization of UNC-13/RIM regulates synaptic vesicle release probability but not priming in *C. elegans*. *eLife*. 8:e40585. <https://doi.org/10.7554/eLife.40585>

- Luo, F., T. Bacaj, and T.C. Südhof. 2015. Synaptotagmin-7 Is Essential for Ca²⁺-Triggered Delayed Asynchronous Release But Not for Ca²⁺-Dependent Vesicle Priming in Retinal Ribbon Synapses. *J. Neurosci.* 35:11024–11033. <https://doi.org/10.1523/JNEUROSCI.0759-15.2015>
- Mackler, J.M., J.A. Drummond, C.A. Loewen, I.M. Robinson, and N.E. Reist. 2002. The C(2)B Ca(2+)-binding motif of synaptotagmin is required for synaptic transmission in vivo. *Nature.* 418:340–344. <https://doi.org/10.1038/nature00846>
- Matthew, W.D., L. Tsavaler, and L.F. Reichardt. 1981. Identification of a synaptic vesicle-specific membrane protein with a wide distribution in neuronal and neurosecretory tissue. *J. Cell Biol.* 91:257–269. <https://doi.org/10.1083/jcb.91.1.257>
- Maximov, A., Y. Lao, H. Li, X. Chen, J. Rizo, J.B. Sørensen, and T.C. Südhof. 2008. Genetic analysis of synaptotagmin-7 function in synaptic vesicle exocytosis. *Proc. Natl. Acad. Sci. USA.* 105:3986–3991. <https://doi.org/10.1073/pnas.0712372105>
- McEwen, J.M., J.M. Madison, M. Dybbs, and J.M. Kaplan. 2006. Antagonistic regulation of synaptic vesicle priming by Tomosyn and UNC-13. *Neuron.* 51:303–315. <https://doi.org/10.1016/j.neuron.2006.06.025>
- Mullen, G.P., K.M. Grundahl, M. Gu, S. Watanabe, R.J. Hobson, J.A. Crowell, J.R. McManus, E.A. Mathews, E.M. Jorgensen, and J.B. Rand. 2012. UNC-41/stonin functions with AP2 to recycle synaptic vesicles in *Caenorhabditis elegans*. *PLoS One.* 7:e40095. <https://doi.org/10.1371/journal.pone.0040095>
- Nishiki, T., and G.J. Augustine. 2004. Synaptotagmin I synchronizes transmitter release in mouse hippocampal neurons. *J. Neurosci.* 24:6127–6132. <https://doi.org/10.1523/JNEUROSCI.1563-04.2004>
- Okada, Y., H. Yamazaki, Y. Sekine-Aizawa, and N. Hirokawa. 1995. The neuron-specific kinesin superfamily protein KIF1A is a unique monomeric motor for anterograde axonal transport of synaptic vesicle precursors. *Cell.* 81:769–780. [https://doi.org/10.1016/0092-8674\(95\)90538-3](https://doi.org/10.1016/0092-8674(95)90538-3)
- Otsuka, A.J., A. Jeyaparakash, J. García-Añoveros, L.Z. Tang, G. Fisk, T. Hartshorne, R. Franco, and T. Born. 1991. The *C. elegans* unc-104 gene encodes a putative kinesin heavy chain-like protein. *Neuron.* 6:113–122. [https://doi.org/10.1016/0896-6273\(91\)90126-K](https://doi.org/10.1016/0896-6273(91)90126-K)
- Pang, Z.P., J. Sun, J. Rizo, A. Maximov, and T.C. Südhof. 2006. Genetic analysis of synaptotagmin 2 in spontaneous and Ca²⁺-triggered neurotransmitter release. *EMBO J.* 25:2039–2050. <https://doi.org/10.1038/sj.emboj.7601103>
- Pang, Z.P., T. Bacaj, X. Yang, P. Zhou, W. Xu, and T.C. Südhof. 2011. Doc2 supports spontaneous synaptic transmission by a Ca(2+)-independent mechanism. *Neuron.* 70:244–251. <https://doi.org/10.1016/j.neuron.2011.03.011>
- Perin, M.S., V.A. Fried, G.A. Mignery, R. Jahn, and T.C. Südhof. 1990. Phospholipid binding by a synaptic vesicle protein homologous to the regulatory region of protein kinase C. *Nature.* 345:260–263. <https://doi.org/10.1038/345260a0>
- Phillips, A.M., M. Smith, M. Ramaswami, and L.E. Kelly. 2000. The products of the *Drosophila* stoned locus interact with synaptic vesicles via synaptotagmin. *J. Neurosci.* 20:8254–8261. <https://doi.org/10.1523/JNEUROSCI.20-22-08254.2000>
- Reist, N.E., J. Buchanan, J. Li, A. DiAntonio, E.M. Buxton, and T.L. Schwarz. 1998. Morphologically docked synaptic vesicles are reduced in synaptotagmin mutants of *Drosophila*. *J. Neurosci.* 18:7662–7673. <https://doi.org/10.1523/JNEUROSCI.18-19-07662.1998>
- Richmond, J.E., W.S. Davis, and E.M. Jorgensen. 1999. UNC-13 is required for synaptic vesicle fusion in *C. elegans*. *Nat. Neurosci.* 2:959–964. <https://doi.org/10.1038/14755>
- Ritter, B., S. Murphy, H. Dokainish, M. Girard, M.V. Gudheti, G. Kozlov, M. Halin, J. Philie, E.M. Jorgensen, K. Gehring, and P.S. McPherson. 2013. NECA1 regulates AP-2 interactions to control vesicle size, number, and cargo during clathrin-mediated endocytosis. *PLoS Biol.* 11:e1001670. <https://doi.org/10.1371/journal.pbio.1001670>
- Rizo, J., and C. Rosenmund. 2008. Synaptic vesicle fusion. *Nat. Struct. Mol. Biol.* 15:665–674. <https://doi.org/10.1038/nsmb.1450>
- Rosenmund, C., and C.F. Stevens. 1996. Definition of the readily releasable pool of vesicles at hippocampal synapses. *Neuron.* 16:1197–1207. [https://doi.org/10.1016/S0896-6273\(00\)80146-4](https://doi.org/10.1016/S0896-6273(00)80146-4)
- Ruhl, D.A., E. Bomba-Warczak, E.T. Watson, M.M. Bradberry, T.A. Peterson, T. Basu, A. Frelka, C.S. Evans, J.S. Briguglio, T. Basta, et al. 2019. Synaptotagmin 17 controls neurite outgrowth and synaptic physiology via distinct cellular pathways. *Nat. Commun.* 10:3532. <https://doi.org/10.1038/s41467-019-11459-4>
- Schivell, A.E., S. Mochida, P. Kensel-Hammes, K.L. Custer, and S.M. Bajjalieh. 2005. SV2A and SV2C contain a unique synaptotagmin-binding site. *Mol. Cell. Neurosci.* 29:56–64. <https://doi.org/10.1016/j.mcn.2004.12.011>
- Schonn, J.S., A. Maximov, Y. Lao, T.C. Südhof, and J.B. Sørensen. 2008. Synaptotagmin-1 and -7 are functionally overlapping Ca²⁺ sensors for exocytosis in adrenal chromaffin cells. *Proc. Natl. Acad. Sci. USA.* 105:3998–4003. <https://doi.org/10.1073/pnas.0712373105>
- Schuske, K.R., J.E. Richmond, D.S. Matthies, W.S. Davis, S. Runz, D.A. Rube, A.M. van der Bliek, and E.M. Jorgensen. 2003. Endophilin is required for synaptic vesicle endocytosis by localizing synaptotagmin. *Neuron.* 40:749–762. [https://doi.org/10.1016/S0896-6273\(03\)00667-6](https://doi.org/10.1016/S0896-6273(03)00667-6)
- Staunton, J., B. Ganetzky, and M.L. Nonet. 2001. Rabphilin potentiates soluble N-ethylmaleimide sensitive factor attachment protein receptor function independently of rab3. *J. Neurosci.* 21:9255–9264. <https://doi.org/10.1523/JNEUROSCI.21-23-09255.2001>
- Stevens, C.F., and J.M. Sullivan. 2003. The synaptotagmin C2A domain is part of the calcium sensor controlling fast synaptic transmission. *Neuron.* 39:299–308. [https://doi.org/10.1016/S0896-6273\(03\)00432-X](https://doi.org/10.1016/S0896-6273(03)00432-X)
- Südhof, T.C. 2012. Calcium control of neurotransmitter release. *Cold Spring Harb. Perspect. Biol.* 4:a011353. <https://doi.org/10.1101/cshperspect.a011353>
- Sugita, S., W. Han, S. Butz, X. Liu, R. Fernández-Chacón, Y. Lao, and T.C. Südhof. 2001. Synaptotagmin VII as a plasma membrane Ca(2+) sensor in exocytosis. *Neuron.* 30:459–473. [https://doi.org/10.1016/S0896-6273\(01\)00290-2](https://doi.org/10.1016/S0896-6273(01)00290-2)
- Sutton, R.B., B.A. Davletov, A.M. Berghuis, T.C. Südhof, and S.R. Sprang. 1995. Structure of the first C2 domain of synaptotagmin I: a novel Ca²⁺/phospholipid-binding fold. *Cell.* 80:929–938. [https://doi.org/10.1016/0092-8674\(95\)90296-1](https://doi.org/10.1016/0092-8674(95)90296-1)
- Turecek, J., S.L. Jackman, and W.G. Regehr. 2017. Synaptotagmin 7 confers frequency invariance onto specialized depressing synapses. *Nature.* 551:503–506. <https://doi.org/10.1038/nature24474>
- Verhage, M., and J.B. Sørensen. 2008. Vesicle docking in regulated exocytosis. *Traffic.* 9:1414–1424. <https://doi.org/10.1111/j.1600-0854.2008.00759.x>
- Wang, P., M.C. Chicka, A. Bhalla, D.A. Richards, and E.R. Chapman. 2005. Synaptotagmin VII is targeted to secretory organelles in PC12 cells, where it functions as a high-affinity calcium sensor. *Mol. Cell. Biol.* 25:8693–8702. <https://doi.org/10.1128/MCB.25.19.8693-8702.2005>
- Wang, W., M. Bouhours, E.O. Gracheva, E.H. Liao, K. Xu, A.S. Sengar, X. Xin, J. Roder, C. Boone, J.E. Richmond, et al. 2008. ITSN-1 controls vesicle recycling at the neuromuscular junction and functions in parallel with DAB-1. *Traffic.* 9:742–754. <https://doi.org/10.1111/j.1600-0854.2008.00712.x>
- Wang, Z., H. Liu, Y. Gu, and E.R. Chapman. 2011. Reconstituted synaptotagmin I mediates vesicle docking, priming, and fusion. *J. Cell Biol.* 195:1159–1170. <https://doi.org/10.1083/jcb.201104079>
- Weber, J.P., T.L. Toft-Bertelsen, R. Mohrmann, I. Delgado-Martinez, and J.B. Sørensen. 2014. Synaptotagmin-7 is an asynchronous calcium sensor for synaptic transmission in neurons expressing SNAP-23. *PLoS One.* 9:e114033. <https://doi.org/10.1371/journal.pone.0114033>
- Weimer, R.M., E.O. Gracheva, O. Meyrignac, K.G. Miller, J.E. Richmond, and J.L. Bessereau. 2006. UNC-13 and UNC-10/rim localize synaptic vesicles to specific membrane domains. *J. Neurosci.* 26:8040–8047. <https://doi.org/10.1523/JNEUROSCI.2350-06.2006>
- Wen, H., M.W. Linhoff, M.J. McGinley, G.L. Li, G.M. Corson, G. Mandel, and P. Brehm. 2010. Distinct roles for two synaptotagmin isoforms in synchronous and asynchronous transmitter release at zebrafish neuromuscular junction. *Proc. Natl. Acad. Sci. USA.* 107:13906–13911. <https://doi.org/10.1073/pnas.1008598107>
- White, J.G., E. Southgate, J.N. Thomson, and S. Brenner. 1986. The structure of the nervous system of the nematode *Caenorhabditis elegans*. *Philos. Trans. R. Soc. Lond. B Biol. Sci.* 314:1–340. <https://doi.org/10.1098/rstb.1986.0056>
- Wu, D., T. Bacaj, W. Morishita, D. Goswami, K.L. Arendt, W. Xu, L. Chen, R.C. Malenka, and T.C. Südhof. 2017. Postsynaptic synaptotagmins mediate AMPA receptor exocytosis during LTP. *Nature.* 544:316–321. <https://doi.org/10.1038/nature21720>
- Xu, J., T. Mashimo, and T.C. Südhof. 2007. Synaptotagmin-1, -2, and -9: Ca(2+) sensors for fast release that specify distinct presynaptic properties in subsets of neurons. *Neuron.* 54:567–581. <https://doi.org/10.1016/j.neuron.2007.05.004>
- Xu, J., Z.P. Pang, O.H. Shin, and T.C. Südhof. 2009. Synaptotagmin-1 functions as a Ca²⁺ sensor for spontaneous release. *Nat. Neurosci.* 12:759–766. <https://doi.org/10.1038/nn.2320>
- Yao, J., J.D. Gaffaney, S.E. Kwon, and E.R. Chapman. 2011. Doc2 is a Ca²⁺ sensor required for asynchronous neurotransmitter release. *Cell.* 147:666–677. <https://doi.org/10.1016/j.cell.2011.09.046>

- Yoshihara, M., and J.T. Littleton. 2002. Synaptotagmin I functions as a calcium sensor to synchronize neurotransmitter release. *Neuron*. 36:897–908. [https://doi.org/10.1016/S0896-6273\(02\)01065-6](https://doi.org/10.1016/S0896-6273(02)01065-6)
- Yoshihara, M., Z. Guan, and J.T. Littleton. 2010. Differential regulation of synchronous versus asynchronous neurotransmitter release by the C2 domains of synaptotagmin I. *Proc. Natl. Acad. Sci. USA*. 107:14869–14874. <https://doi.org/10.1073/pnas.1000606107>
- Yu, S.C., S.M. Klosterman, A.A. Martin, E.O. Gracheva, and J.E. Richmond. 2013. Differential roles for snapin and synaptotagmin in the synaptic vesicle cycle. *PLoS One*. 8:e57842. <https://doi.org/10.1371/journal.pone.0057842>
- Zhang, B., Y.H. Koh, R.B. Beckstead, V. Budnik, B. Ganetzky, and H.J. Bellen. 1998. Synaptic vesicle size and number are regulated by a clathrin adaptor protein required for endocytosis. *Neuron*. 21:1465–1475. [https://doi.org/10.1016/S0896-6273\(00\)80664-9](https://doi.org/10.1016/S0896-6273(00)80664-9)
- Zhang, X., M.J. Kim-Miller, M. Fukuda, J.A. Kowalchuk, and T.F. Martin. 2002. Ca²⁺-dependent synaptotagmin binding to SNAP-25 is essential for Ca²⁺-triggered exocytosis. *Neuron*. 34:599–611. [https://doi.org/10.1016/S0896-6273\(02\)00671-2](https://doi.org/10.1016/S0896-6273(02)00671-2)

Supplemental material

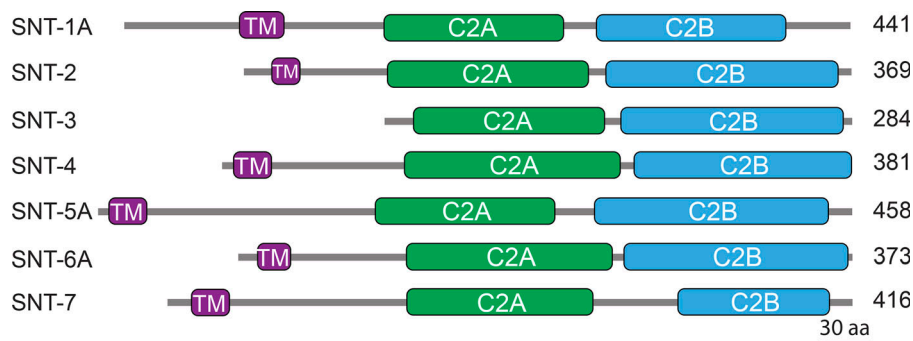


Figure S1. **Domain structure of the seven Syt genes in *C. elegans*.** The TM domain and the C2 domains (C2A and C2B) in each Syt isoform are indicated.

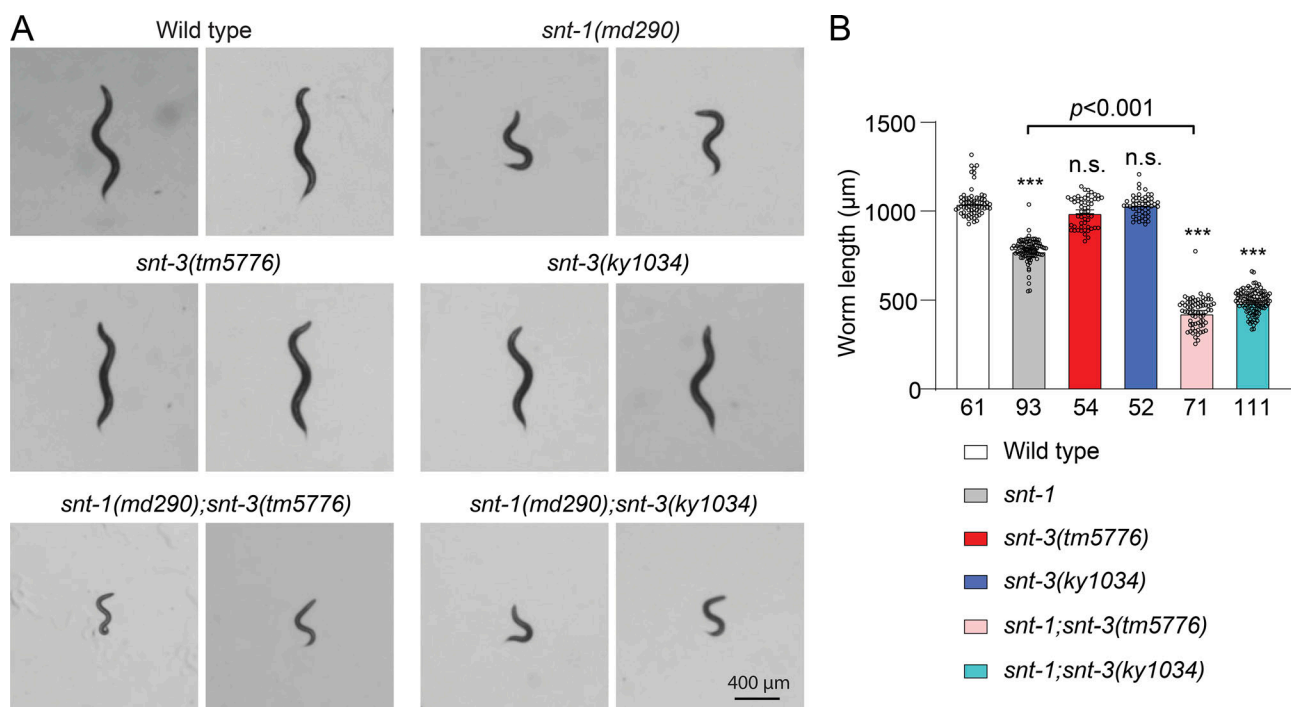


Figure S2. **The loss of both SNT-1 and SNT-3 leads to dramatically shorter body length.** (A) Representative worm images from indicated genotypes, including WT, *snt-1*, *snt-3(tm5776)*, *snt-3(ky1034)*, *snt-1;snt-3(tm5776)*, and *snt-1;snt-3(ky1034)*. Scale bar, 400 µm. (B) Quantification of body length. Body length was measured by using WormLab software. Data are mean ± SEM. ***P < 0.001 compared with WT. n.s., nonsignificant compared with WT (one-way ANOVA).

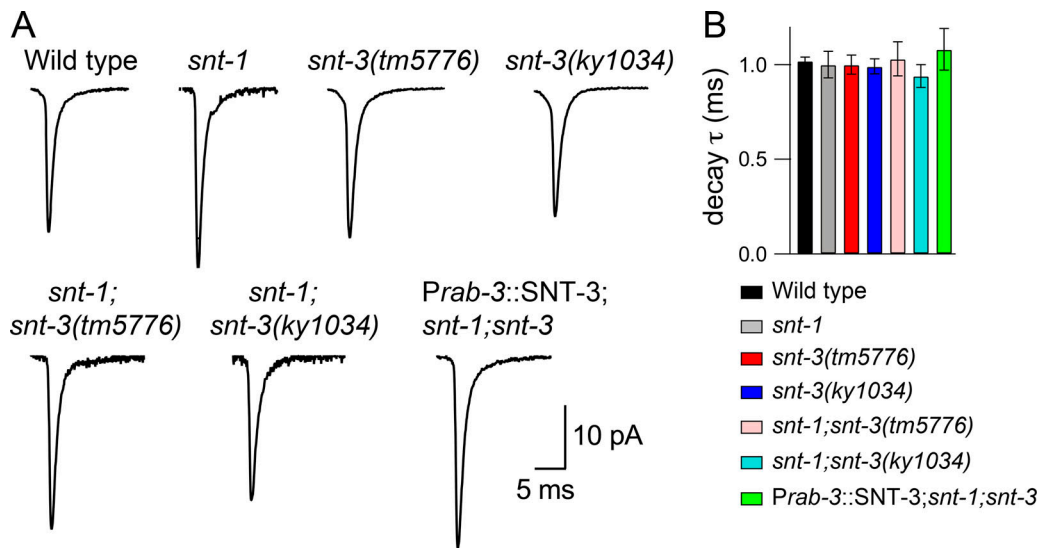


Figure S3. **The loss of *snt-1* or *snt-3* does not alter mEPSC decay.** (A) Representative mEPSC traces from the indicated genotypes. (B) Quantification of mEPSC decay from the same genotypes in A. Data are mean \pm SEM.

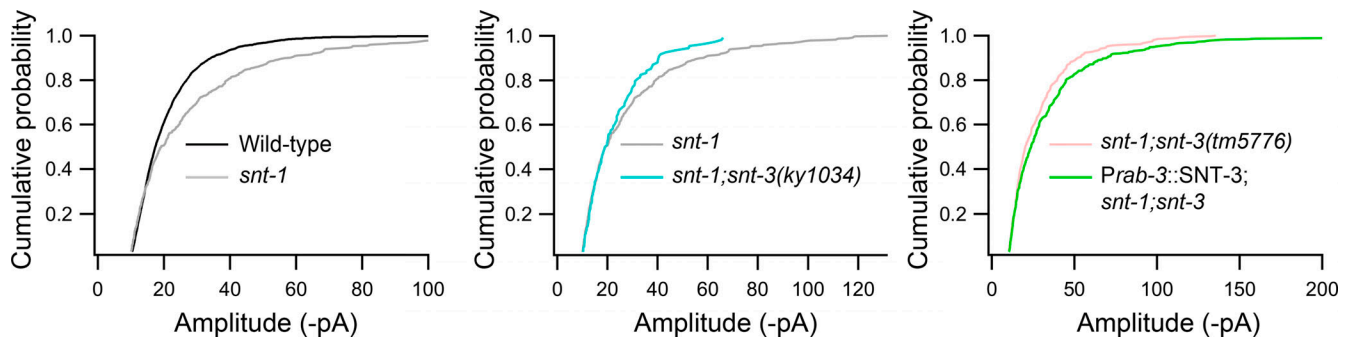


Figure S4. **SNT-1 and SNT-3 alter mEPSC amplitude.** Cumulative probability distributions of mEPSC amplitude from the indicated genotypes and trans-genes, including WT, *snt-1*, *snt-1;snt-3(tm5776)*, *snt-1;snt-3(ky1034)*, and SNT-3 overexpression rescue.

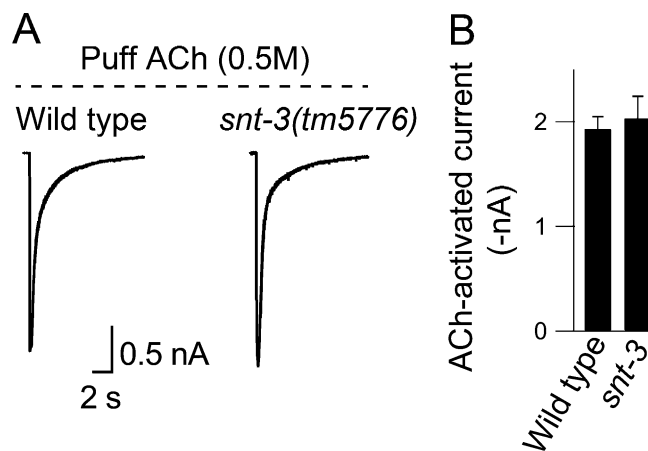


Figure S5. **Body wall muscles respond normally to ACh in *snt-3* mutants.** (A) Example traces of puff ACh-activated currents in WT and *snt-3* mutants. (B) Quantification of current amplitude in A. Data are mean \pm SEM.

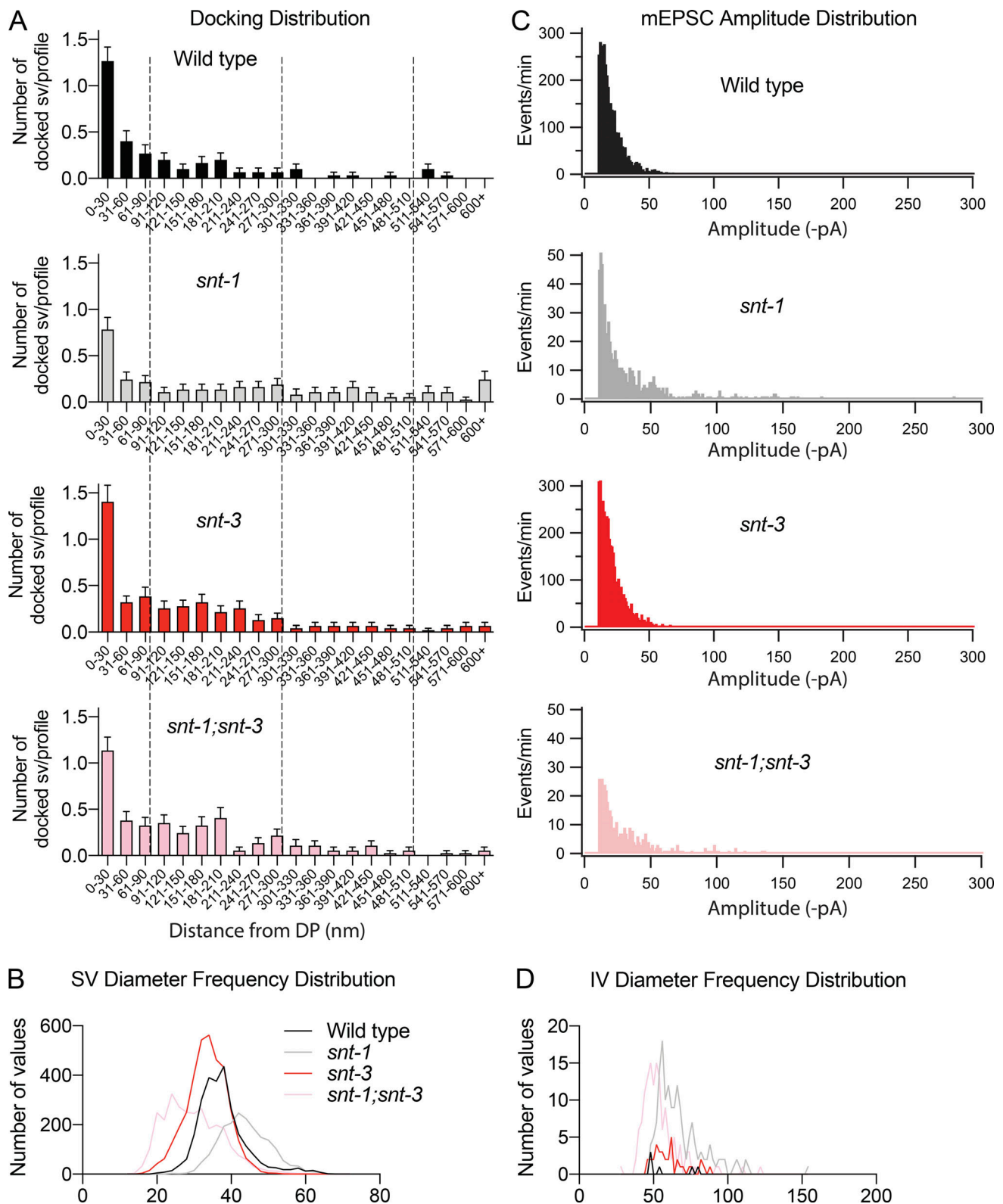


Figure S6. **Differential roles of SNT-1 and SNT-3 in docking and vesicle size.** (A) Distribution of docked vesicles as a measure of distance from the DP (nm) in 30-nm bins. Vesicles docked within 90 nm of the DP are considered proximal, vesicles docked 91–300 nm from the DP are considered distal, and vesicles docked from 301–510 nm from the DP are considered to be docked within the endocytic zone. (B) Frequency distribution of SV diameters. *snt-1* mutants show a right shift in the frequency of SV diameter, *snt-3* mutants show a left shift in the frequency of SV diameter, which is further shifted in the *snt-1;snt-3* double mutants. (C) mEPSC amplitude histograms from indicated genotypes. (D) Frequency distribution of irregular vesicle (IV) diameters. *snt-1* mutants show a right shift in the frequency of irregular vesicle diameter, whereas *snt-1;snt-3* double mutants show a right shift in the diameter distribution of irregular vesicle diameter.

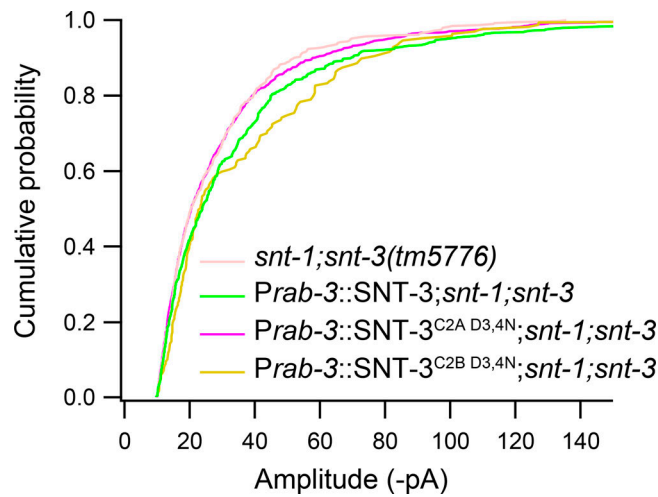


Figure S7. **Effects of overexpression of WT or mutated SNT-3 on mEPSC amplitude in *snt-1;snt-3* double mutants.** Cumulative probability distributions of mEPSC amplitude from the indicated genotypes and transgenes, including WT, *snt-1*, *snt-1;snt-3(tm5776)*, *snt-1;snt-3(ky1034)*, and SNT-3 overexpression rescue.

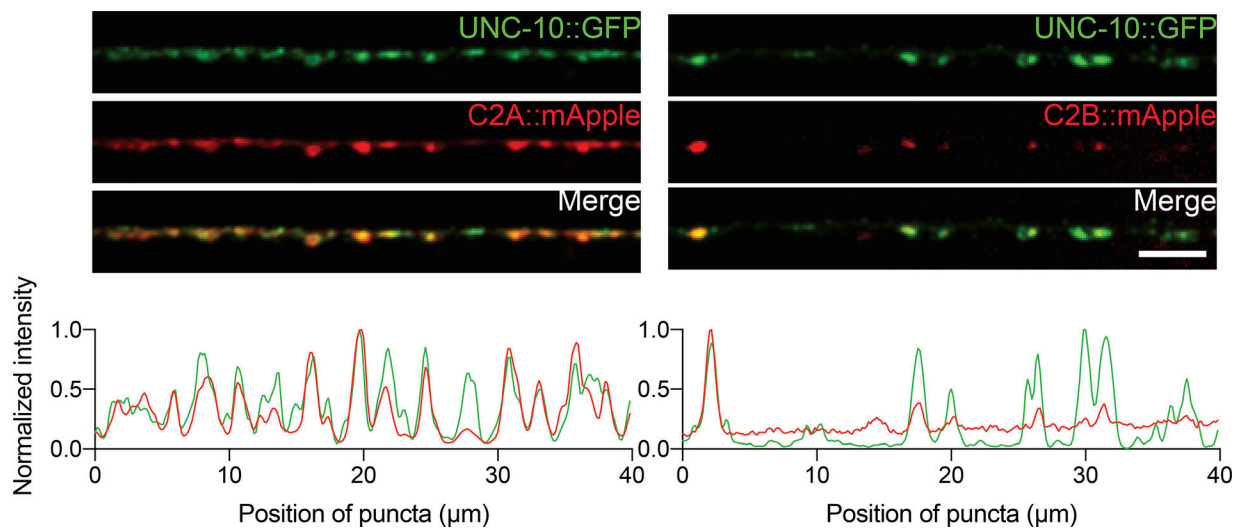


Figure S8. **The individual C2A and C2B domains of SNT-1 are localized at active zones.** The mApple-tagged C2A or C2B domain of SNT-1 are expressed in the D-type cholinergic motor neurons (under the *unc-129* promoter). They both exhibit well colocalization with the active zone marker UNC-10::GFP. (Upper) Representative images of UNC-10::GFP, C2A::mApple, and C2B::mApple. (Bottom) Line scans along the dorsal nerve cord. Scale bar, 5 μ m.

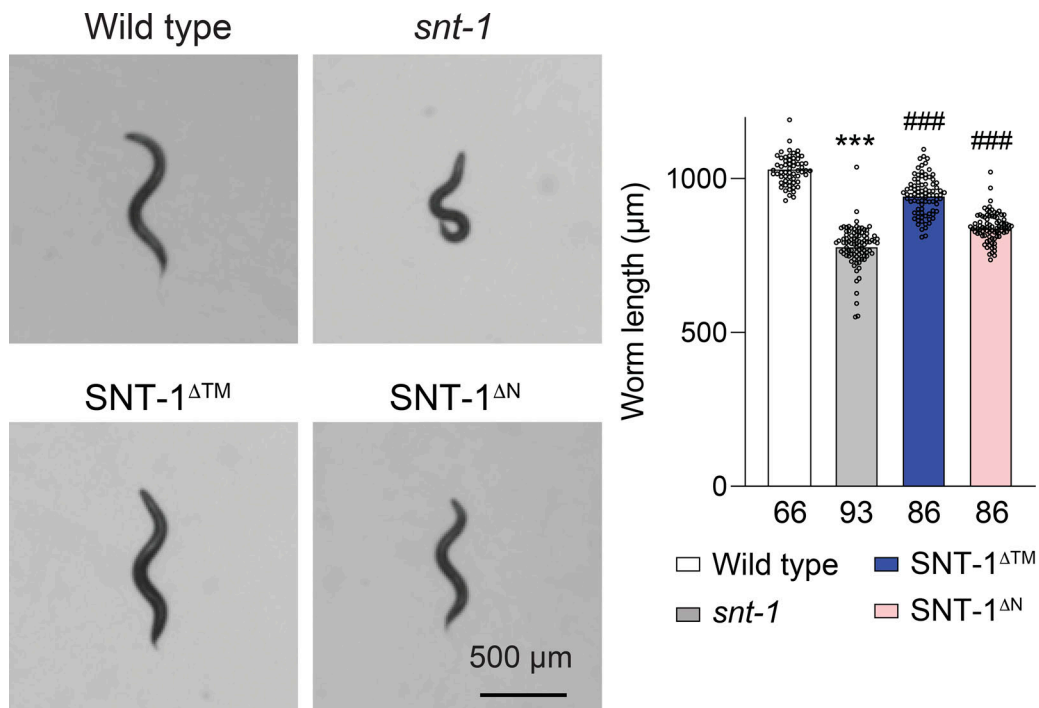


Figure S9. **Cytoplasmic SNT-1 significantly rescued body length in *snt-1* mutants.** (Left) Representative worm images from indicated genotypes, including WT, *snt-1*, and SNT-1^{ΔTM} and SNT-1^{ΔN} rescue worms. Scale bar, 500 μm. (Right) Quantification of body length. Body length was measured by using WormLab software. Data are mean ± SEM. ***P < 0.001 compared with WT; ###P < 0.001 compared with *snt-1* mutants (one-way ANOVA).

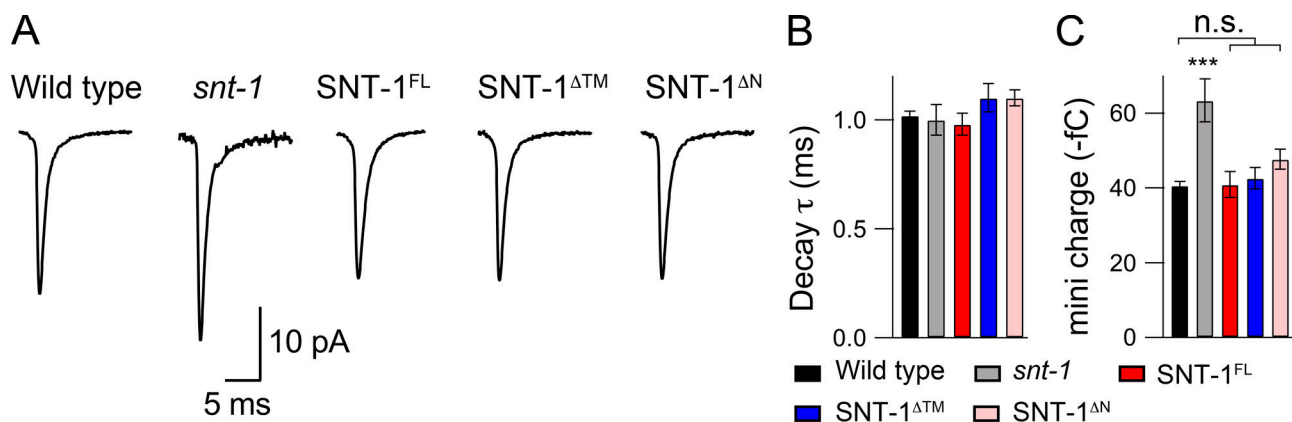


Figure S10. **Deleting the TM domain or the whole N terminus in SNT-1 does not alter the mEPSC decay.** (A) Representative mEPSC traces from the indicated genotypes and transgenes. (B and C) Quantification of mEPSC decay and charge from the same genotypes in A. Data are mean ± SEM. ***P < 0.001 compared with WT. n.s., nonsignificant (one-way ANOVA).

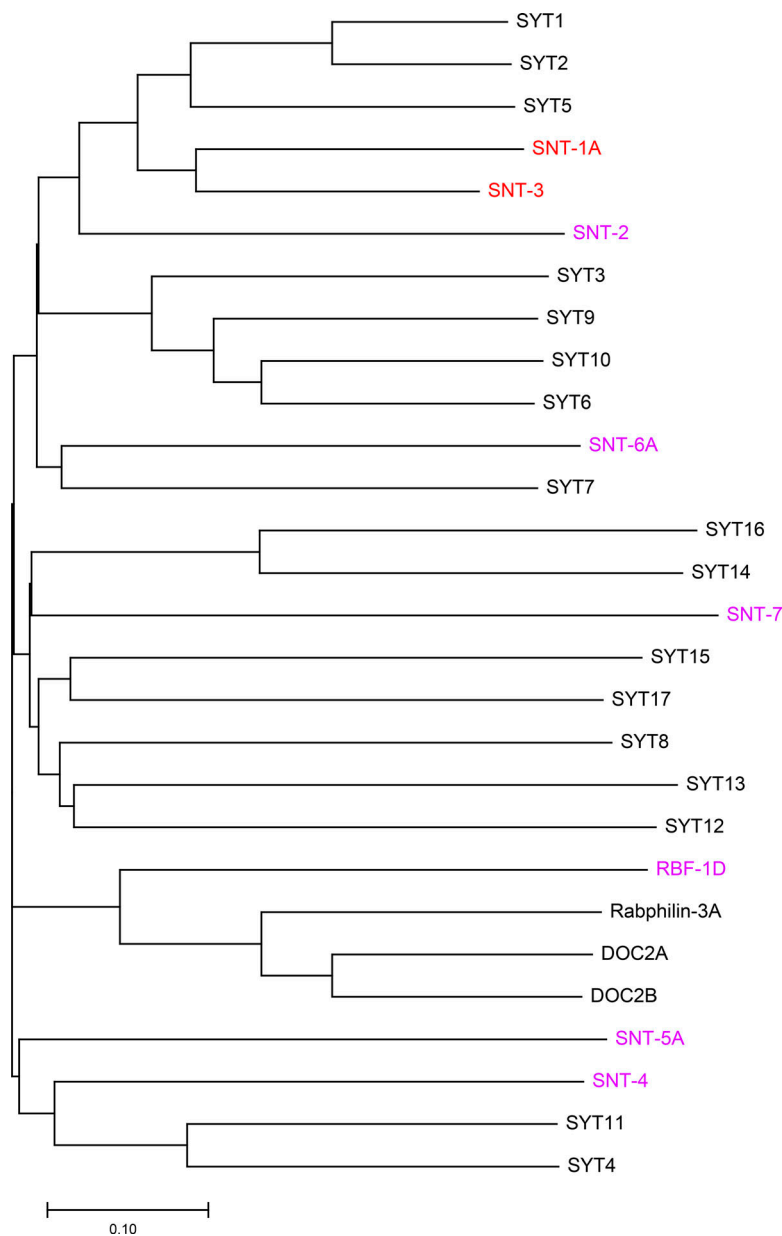


Figure S11. **Phylogenetic tree of worm and mouse Syts.** Sequences were aligned by using clustal omega with default parameters, and the phylogenetic tree was created with MEGA-X (Molecular Evolutionary Genetics Analysis).

Table S1 is provided online and summarizes the electrophysiological data in this study.